

A First Transients Survey with JWST: the FLARE project

Lifan Wang, D. Baade, E. Baron, S. Bernard, V. Bromm, P. Brown , G. Clayton, J. Cooke,
D. Croton, C. Curtin, M. Drout, M. Doi, I. Dominguez, S. Finkelstein, A. Gal-Yam , P.
Geil, A. Heger, P. Hoefflich, J. Jiang, K. Krisciunas, A. Koekemoer, R. Lunnan, K. Maeda,
J. Maund, M. Modjaz, J. Mould, K. Nomoto, P. Nugent, F. Patat, F. Pacucci, M. Phillips,
A. Rest, E. Regos, D. Sand, B. Sparks, J. Spyromilio, L. Staveley-Smith, N. Suntzeff, S.
Uddin, B. Villarroel, J. Vinko, D. Whalen, J. Wheeler, M. Wood-Vasey, Xiaofeng Wu, Y.

Yang, & Bin Yue

Received _____; accepted _____

ABSTRACT

The *James Webb Space Telescope (JWST)* was conceived and built to answer one of the most fundamental questions that humans can address empirically: “How did the Universe make its first stars?”. This can be attempted in classical stare mode and by still photography - with all the pitfalls of crowding and multi-band redshifts of objects of which a spectrum was never obtained. Our First Lights At REionization (FLARE) project transforms the quest for the epoch of reionization from the static to the time domain. It targets the complementary question: “What happened to those first stars?”. It will be answered by observations of the most luminous events: supernovae and accretion on to black holes formed by direct collapse from the primordial gas clouds. These transients provide direct constraints on star-formation rates and the truly initial initial mass function, and they may identify possible stellar seeds of supermassive black holes. Furthermore, our knowledge of the physics of these events at ultra-low metallicity will be much expanded. *JWST*'s unique capabilities will detect these most luminous and earliest cosmic messengers easily in fairly shallow observations. However, these events are very rare at the dawn of cosmic structure formation and so require large area coverage. Time domain astronomy can be advanced to an unprecedented depth by means of a shallow field of *JWST* reaching 27 mag (AB) in 2 μm and 4.4 μm over a field as large as 0.1 square degree visited multiple times each year. Such a survey may set strong constraints or detect massive Population III supernovae at redshifts beyond 10, pinpointing the redshift of the first stars, or at least their death. Based on our current knowledge of superluminous supernovae, such a survey will find one or more superluminous supernovae at redshifts above 6 in five years and possibly several direct collapse black holes. In addition, the large scale structure that is the trademark of the epoch of reion-

ization will be detected. Although *JWST* is not designed as a wide field survey telescope, we show that such a wide field survey is possible with *JWST* and is critical in addressing several of its key scientific goals.

Subject headings: astronomical instrumentation, methods, techniques – surveys — stars: Population III – supernovae: general –dark ages, reionization, first stars – quasars: supermassive black holes

Contents

1	Introduction	5
1.1	The Epoch of First Light	6
1.2	Current candidate first galaxies and Ly α blobs	7
1.3	AGN Variability	8
2	Transient Survey Science Goals	10
2.1	Population III Supernovae	10
2.1.1	Probing Pop III with Transients	11
2.1.2	Finding the First Supernovae	11
2.1.3	Observational constraints	15
2.1.4	Modelled high-redshift SLSNe rates	17
2.1.5	Normal SNe	20
2.1.6	SN rates	25
2.1.7	Finding the First Type Ia SNe	28
2.2	Large Scale Structure in the Epoch of Reionization	28
2.3	Growing supermassive black holes before Reionization	31
2.3.1	The brightness, number density and detectability of DCBHs	33
2.3.2	The infrared colors of DCBHs	36
2.4	Serendipitous high-redshift transients	39

2.4.1	Kilonovae	39
2.4.2	Formation of globular clusters	42
3	The FLARE <i>JWST</i> Transient Field	42
3.1	Why cluster lensing does not help find more transients	43
3.2	Probabilistic Target Classification	44
3.2.1	Brown dwarfs	45
4	Facilitating First Transients discovery	46
4.1	The design of the FLARE project	46
4.1.1	Observations and deliverables with <i>JWST</i>	46
4.1.2	Supporting observations and followup strategies	47
5	Conclusion	48

1. Introduction

Just as a famous early goal of the *Hubble Space Telescope* (*HST*) was to measure the Hubble Constant, so a well publicized early goal of the *James Webb Space Telescope* (*JWST*) is to find and characterize the first stars in the Universe. Population III (Pop III) does not come with a handbook of how to do this. In a ‘shallow’ survey, *JWST* takes us into a discovery space of transient phenomena at AB ~ 27 mag of which we have no knowledge. The community needs to know about transient phenomena in the very early Universe, as transients are prompt tracers of the constituents of the Universe. This knowledge may

affect the subsequent mission in significant ways.

Supernovae (SNe) are the defining characteristic of Pop III. When the first SNe occur, Pop III ends, because they inject first metals into the intergalactic medium. *Inter alia* the early science with *JWST* can recognize the first supernovae by their rise time. If this can be achieved, a wealth of follow up science opens up for the community, not fully predictable at the time of launch, but possibly among the major outcomes of the mission.

In this paper we consider in turn survey science goals (§2), a 0.1 square degree field survey for transients with *JWST* (§3), and facility deliverables to allow community use of the survey (§4). We draw our conclusions in §5, leaving detailed simulations for a subsequent paper.

1.1. The Epoch of First Light

A key gap in our understanding of cosmic history is the pre-reionization Universe, comprising the first billion years of cosmic evolution (Bromm & Yoshida 2011; Loeb & Furlanetto 2013). Within Λ CDM cosmology, we have an increasingly detailed theoretical picture of how the first stars and galaxies brought about the end of the cosmic dark ages, initiating the process of reionization (Barkana & Loeb 2007; Robertson et al. 2010), and endowing the primordial universe with the first heavy chemical elements (Karlsson et al. 2013). The initial conditions for primordial star formation are known to very high precision by probing the spectrum of primordial density fluctuations imprinted in the cosmic microwave background (CMB), carried out by *WMAP* and *Planck*. The first stars thus mark the end of precision cosmology, and their properties are closely linked to the cosmological initial conditions.

We are entering the exciting period of testing our predictions about the first stars and

galaxies with a suite of upcoming, next-generation telescopes. Soon, *JWST* will provide unprecedented imaging sensitivity in the near- and mid-IR, to be followed by the 30–40 m class, ground-based telescopes now under development. In addition, astronomers will bring to bear facilities that can probe the cold Universe at these early times. Next to the ALMA observatory, a suite of meter-wavelength radio interferometers are being built that will probe the redshifted 21-cm radiation, emitted by the neutral hydrogen at the end of the cosmic dark ages (Furlanetto et al. 2006). The radio facilities provide a view of the raw material, the cold primordial hydrogen gas, out of which the first stars form. In addition, there are missions that aim at discovering transients originating in the violent deaths of the first stars. A prime example is the search for high-redshift gamma-ray bursts (GRBs), marking the death of progenitor stars that are massive enough to collapse into a black hole (Bromm & Loeb 2006; Kumar & Zhang 2015). Overall, the prospects for closing the remaining gap in understanding the entire history of the Universe, including the still elusive first billion years, are bright. This gap is actually a discontinuity in our understanding which prevents us from smoothly connecting the predictions from the earlier epoch of precision cosmology to extrapolations from the local Universe and intermediate redshifts.

1.2. Current candidate first galaxies and Ly α blobs

At the redshift of reionization ($z > 6$), emission lines from distant galaxies become increasingly difficult to observe. The brightest line, Ly α , becomes virtually the only line accessible from the ground. Significant progress has been made in recent years finding luminous Ly α emitters (e.g. Matthee et al. 2015; Ouchi et al. 2010; Sobral et al. 2015).

The best observational evidence on first generation stars or black hole (BH) seeds is found in a distant galaxy CR7 (Figure 1). These identifications rely heavily on theoretical models of the radiation from first stars (e.g., Pallottini et al. 2015; Xu et al.

2016; Yajima & Khochfar 2017) or direct collapse black holes (DCBHs) (e.g. Pacucci et al. 2017; Agarwal et al. 2016, 2017; which was disputed by Bowler et al. 2017).

The spectral energy distribution (SED) of CR7 is shown in Figure 1 (Bowler et al. 2017). A shallow, wide-field survey with *JWST* is sufficiently deep to discover luminous Ly α emitters like CR7. Matthee et al. (2015) found that the luminous end of the luminosity function of Ly α emitters at $z = 6.6$ is comparable to the luminosity function at $z = 3-5.7$, and is consistent with no evolution at the bright end since $z \sim 3$. The number density of luminous Ly α emitters is thus found to be much more common than expected. The space density is $1.4_{-0.7}^{+1.2} \times 10^{-5} \text{ Mpc}^{-3}$. From Figure 1, we see that such targets can be easily discovered in a survey that goes to 27th mag in $2 \mu\text{m}$ and $4.4 \mu\text{m}$. They are characterized by very red colors in this wavelength range. Note, however, Bowler et al. (2017) found a blue $[3.6] - [4.5]$ color based on *Spitzer* data, and argued that CR7 is likely a low-mass, narrow-line active galactic nucleus (AGN) or is associated with a young, low-metallicity ($\sim 1/200 Z_{\odot}$) star-burst.

In the design of FLARE, we expect to discover 20–50 luminous Ly α emitters per unit redshift bin at $z \sim 6-10$ assuming a non-evolving rate of luminous Ly α emitters.

1.3. AGN Variability

Among the high-redshift transients FLARE will detect are AGN. These are signposts to the formation of the supermassive black holes (SMBHs) that we know are catapulted from stellar seeds to $\gtrsim 10^9 M_{\odot}$ in the first half billion years of the Universe. Our comoving volume between redshift 6 and 7 is approximately one million Mpc^3 . If every galaxy with a mass exceeding the Milky Way’s has an SMBH, that volume contains 10^4 SMBH. A signature of these is Tidal Distortion Events (TDEs), manifesting themselves as order of

magnitude flares in rise times of $(1 + z)$ times 30 days. Assuming steady growth between $z = 20$ and $z = 6$, each $10^7 M_{\odot}$ SMBH is adding $0.01 M_{\odot}$ per year. If 10% of this material is stars, the rate of TDEs is of order ten per year. What makes these high-redshift objects detectable, as is also true of superluminous supernovae (SLSNe), is that accretion or shocks make them UV bright, more like flat spectrum sources than the 10,000 K black bodies that normal photosphere-like SNe resemble. Caplar et al. (2016) find that the amplitude of AGN variation in PTF and SDSS is typically a tenth of a magnitude, but, interestingly, this goes up by a factor of 5 in the UV, which is where FLARE will observe at high redshift.

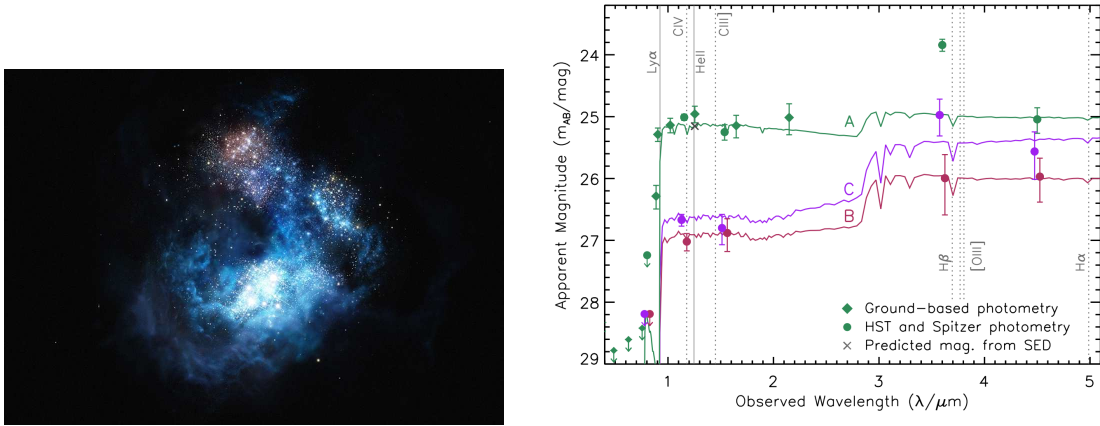


Fig. 1.— Left: COSMOS Redshift 7 (abbreviated to CR7) is a bright galaxy found in the COSMOS field (Matthee et al. 2015; Sobral et al. 2015). Right: The SEDs of the three components of CR7 are plotted in green (A), purple (B) and red (C), together with the best-fitting Bruzual & Charlot (2003) model shown as the solid line in each case. The solid vertical grey lines show the observed wavelengths of the confirmed Ly α and He II emission lines, whereas the dotted vertical lines show for reference the wavelengths of other rest-frame UV and optical lines that have been detected or inferred in other high-redshift Lyman-break galaxies (Stark et al. 2015a,b; de Barros et al. 2016; Smit et al. 2014; Smidt et al. 2016).

2. Transient Survey Science Goals

The purpose of the survey is to find transients as witnesses of the state of the Universe when the first stars and black holes were formed. As we shall see, an appropriate search strategy is a mosaic approach with only modestly deep individual exposures. In §3 a 0.1 square degree field is considered to reach into this wide-field regime and place constraints on the massive Pop III star formation rate density.

2.1. Population III Supernovae

How massive can the first stars, the so-called Population III, grow (Bromm 2013)? This question is important in order to determine the nature of the death of these stars, which in turn governs the feedback exerted by them on their surroundings (Maeder & Meynet 2012). To address it, simulations have to be pushed into the radiation hydrodynamic regime, where protostars more massive than $\sim 10 M_{\odot}$ emit ionizing photons, resulting in the build-up of ultra-compact H II regions (Hosokawa et al. 2011, 2016; Hirano et al. 2014; Stacy et al. 2012). The roughly bi-conical H II regions then begin to photo-evaporate the proto-stellar disk, thus choking off the gas supply for further accretion (McKee & Tan 2008). Upper masses thus reached are typically in the vicinity of a few times $10 M_{\odot}$, such that the most likely fate encountered by the first stars is a core-collapse supernova. On the other hand, the prediction is that the primordial initial mass function (IMF) was rather broad, extending both to lower and (possibly significantly) higher masses. The latter would imply that BH remnants should be quite common as well. In rarer cases pair-instability (PI) SN progenitors would give rise to hyper-energetic explosions. See also Woosley et al. (2002), Heger et al. (2003), Heger & Woosley (2002a), Kasen et al. (2011), and references therein.

2.1.1. Probing Pop III with Transients

Transients are the targets of choice because they are the brightest individual objects, whereas not even the first galaxies are detected in the same observations. Testing Pop III predictions is challenging, given that Pop III stars are short-lived, and that rapid initial enrichment hides Pop III star formation from view, such that even the deepest *JWST* exposures will typically tend to see metal-enriched, Population II, stellar systems. Therefore, a more indirect strategy is required. A promising approach is to constrain the extreme ends of the Pop III IMF. On the high-mass end, the search for PI SNe in upcoming *JWST* surveys will tell us whether primordial star formation led to masses in excess of $\sim 150 M_{\odot}$, the threshold for the onset of the pair-production instability. Individual PI SN events are bright enough to be detected with the *JWST*, but the challenge will be their low surface density, such that a wide area needs to be searched (Hummel et al. 2012; Pan et al. 2012; Whalen et al. 2013f).

2.1.2. Finding the First Supernovae

The cosmic dark ages ended with the formation of the first stars at $z \sim 20$, or ~ 200 Myr after the Big Bang (e.g., Bromm et al. 2009; Bromm & Yoshida 2011; Whalen 2013). The first stars began cosmological reionization (Whalen et al. 2004; Alvarez et al. 2006; Abel et al. 2007), enriched the primeval universe with the first heavy elements (Mackey et al. 2003; Smith & Sigurdsson 2007; Whalen et al. 2008; Joggerst et al. 2010; Safranek-Shrader et al. 2014), populated the first galaxies (Johnson et al. 2009; Pawlik et al. 2011; Wise et al. 2012; O’Shea et al. 2015), and may be the origin of the first SMBHs (Whalen & Fryer 2012; Johnson et al. 2013b; Woods et al. 2017; Smidt et al. 2017). In spite of their importance to the early universe, not much is known about the properties of Pop III stars, as not even *JWST* or 30–40 m class telescopes such as the Giant Magellan

Telescope (GMT), the Thirty-Meter Telescope (TMT), or the Extremely Large Telescope (ELT) will be able to see them (Rydberg et al. 2010). And while the initial conditions for Pop III star formation are well understood, having been constrained by measurements of primordial density fluctuations by both *WMAP* and *Planck*, numerical simulations cannot yet determine the masses of primordial stars from first principles (e.g., Bromm et al. 2009; Bromm & Yoshida 2011; Whalen 2013). However, some of these models suggest that they may have ranged from a few tens of solar masses to $\sim 1000 M_{\odot}$, with a fairly flat distribution in mass (Hirano et al. 2014, 2015; see also Woosley 2017).

High-redshift SNe could directly probe the first generations of stars and their formation rates because they can be observed at great distances and, to some degree, the mass of the progenitor can be inferred from the light curve of the explosion (Tanaka et al. 2013; de Souza et al. 2013, 2014). 1D Lagrangian stellar evolution models (Heger & Woosley 2002b) predict that 8–40 M_{\odot} non-rotating Pop III stars die as core-collapse (CC) SNe and that 40–90 M_{\odot} stars collapse to BHs. If the stars are in rapid rotation, they can produce a GRB (Bromm & Loeb 2006; Mesler et al. 2014) or a hypernova (HN; e.g., Nomoto et al. 2010). 10–40 M_{\odot} stars can also eject shells prior to death, and the subsequent collision of the SN ejecta with the shell can produce highly luminous events that are brighter than the explosion itself (pulsational PI SNe, or PPI SNe; Woosley et al. 2007a; Chen et al. 2014c).

At $\sim 100 M_{\odot}$ non-rotating Pop III stars can encounter the pair instability. At 100–140 M_{\odot} the pair instability causes the ejection of multiple, massive shells instead of the complete destruction of the star (Woosley et al. 2007b). Rotation can cause stars to explode as PI SNe at masses as low as $\sim 85 M_{\odot}$ (rotational PI SNe, or RPI SNe; Chatzopoulos & Wheeler 2012; Yoon et al. 2012; Chatzopoulos et al. 2013). Above 260 M_{\odot} stars encounter photodisintegration with 140–260 M_{\odot} stars exploding as highly energetic thermonuclear PI SNe (Rakavy & Shaviv 1967; Barkat et al. 1967; Joggerst & Whalen

2011; Chen et al. 2014a). Finally, at much higher masses ($\gtrsim 50,000 M_{\odot}$) some stars may die as extremely energetic thermonuclear SNe triggered by the general relativistic instability (Montero et al. 2012; Chen et al. 2014b). Such events could occur in atomically cooled halos at $z \sim 15\text{--}20$, heralding the birth of DCBHs, and thus the first quasars (Johnson et al. 2013a; Whalen et al. 2013d,c,g).

SLSNe can be another critical probe of the deaths of the first stars, because those events are bright ($M < -20.5$ mag) (De Cia et al. 2017; Lunnan et al. 2017) and have UV-luminous SEDs in the rest-frame. SLSNe are typically 2–3 magnitudes brighter than SNe Ia, and 4 or more magnitudes brighter than typical CC SNe. Observationally, there are two known types of SLSNe. Hydrogen-rich SLSN II are thought to gain their extremely high luminosity from the collision between the expanding SN ejecta and a dense circumstellar shell ejected prior to explosion. The mechanism of the explosion itself is less clear, because it is hidden behind the dense circumstellar cloud. Hydrogen-deficient SLSNe, called SLSN I, do not show signs for such a violent collisional interaction, thus, they are thought to be powered by the spin-down of a magnetar resulting from the core collapse of an extremely massive progenitor star (Nicholl et al. 2017).

We have modeled the rest-frame SED of SLSNe I and II using the available data of several well-observed local events (see Figure 2) downloaded from the Weizmann Interactive Supernova Repository¹ and the Open Supernova Catalog². The UV-optical spectra taken close to maximum light, after scaling to match photometry, have been corrected for extinction and distance. Figure 2 shows the final composite spectra together with scaled black bodies that fit the continuum. Since SLSN spectra are not homogeneous, we fit two black bodies having different temperatures and scale factors (plotted with solid and dashed

¹<https://wiserep.weizmann.ac.il/>

²<https://sne.space>

lines, respectively) to represent the range of luminosities for both SLSN types.

In Figure 3 we plot the model SEDs of SLSNe redshifted between $z = 1$ – 10 . It is seen that detection with *JWST* between 2 – $4 \mu\text{m}$ can be feasible for both types even at $z \sim 10$, provided SLSNe do exist at such high redshift. Figure 3 suggests that the detection, in principle, could be pushed above $z = 10$, but time dilation that increases the timescale of transients by a factor of $1 + z$ limits the practical discovery efficiency of the intrinsically slowly evolving SLSNe at such high redshifts.

2.1.3. *Observational constraints*

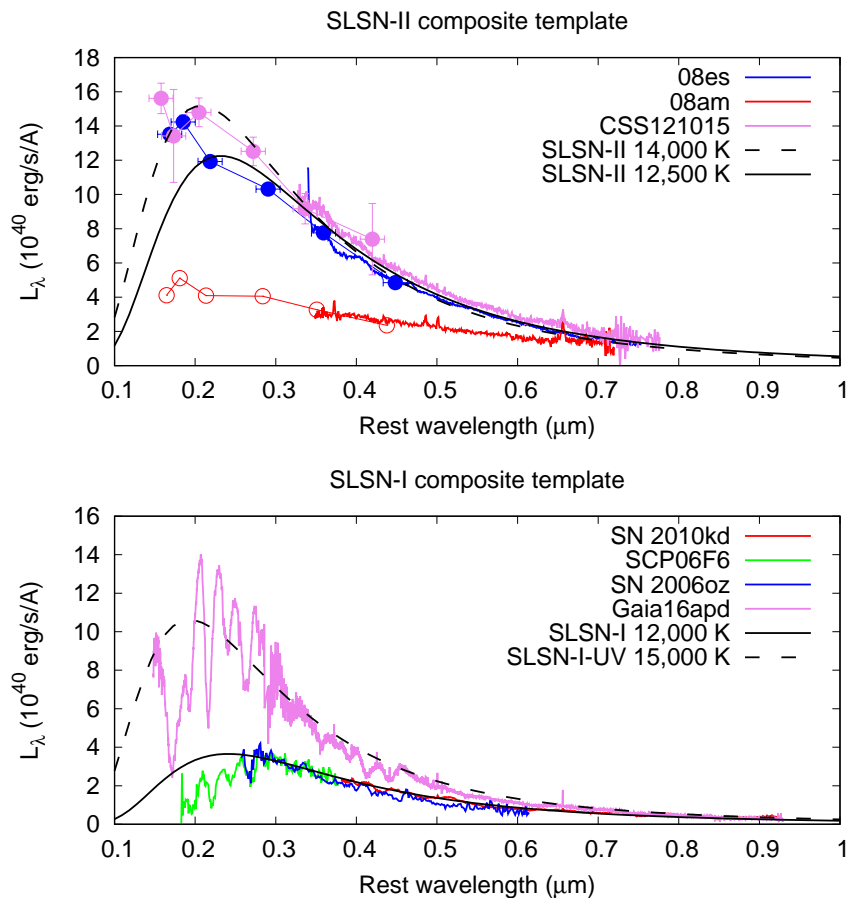


Fig. 2.— The modeled SEDs of SLSNe at maximum light. Hydrogen-rich (SLSN-II) events are plotted in the top panel, while hydrogen-free (SLSN-I) ones are in the bottom panel. The black solid and dotted lines illustrate black body continua that fit the observations.

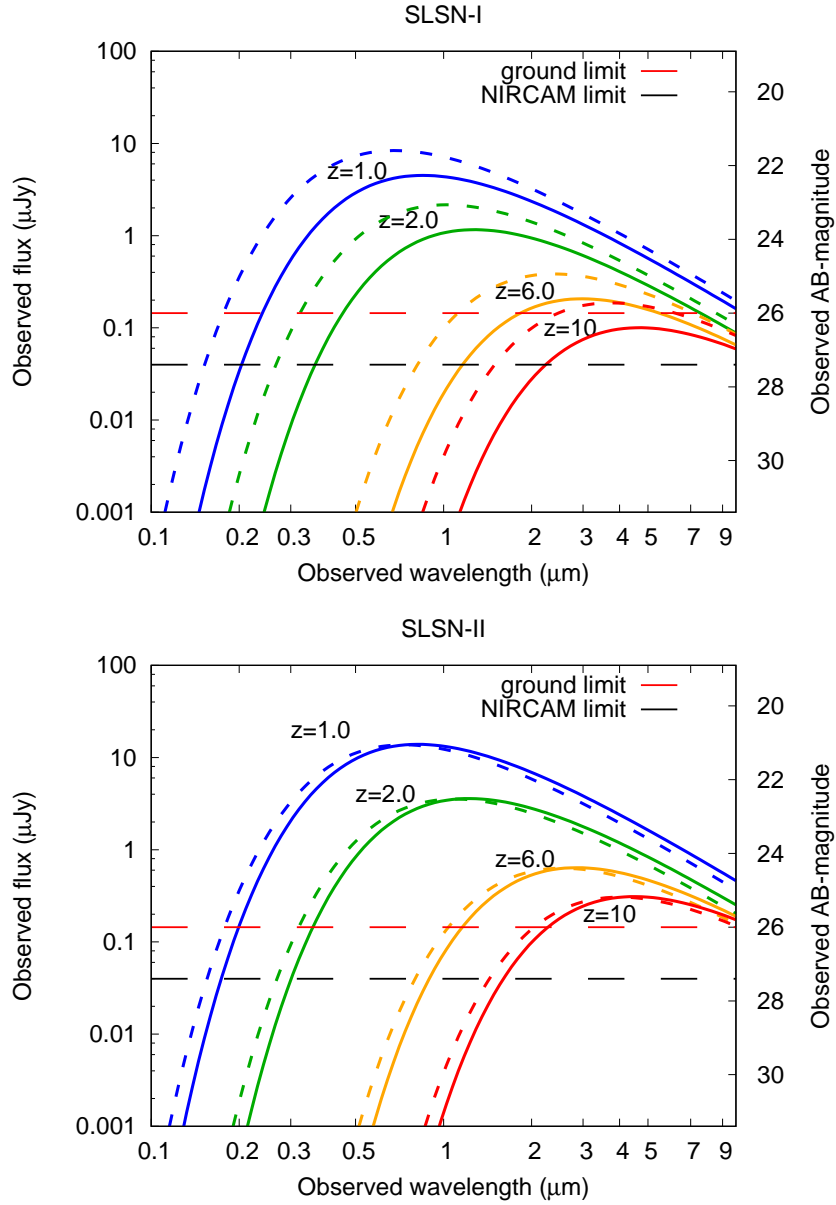


Fig. 3.— The model SEDs of SLSNe (plotted with colored solid and dashed lines) at different redshifts. Top panel: SLSN-I. Lower panel: SLSN-II. The SEDs plotted with dashed lines correspond to the models having higher temperatures (see Figure 2). Dashed red and black horizontal lines represent the detection sensitivity limits from the ground and with *JWST*, respectively.

]

The expected rate of SLSNe beyond $z > 1$ can be estimated from their observed local rates. Locally, SLSNe are rare events. Relatively shallow, flux-limited surveys like CRTS, PTF, and ASASSN discover just a few SLSNe for roughly every 100 normal luminosity SNe. Obviously these surveys can search for SLSNe in much larger effective volumes than for normal luminosity SNe, so the rate of SLSNe is but a fraction of the total SN population’s rate. Quimby et al. (2013) measured a SLSN-like rate of 199_{-86}^{+137} events/Gpc³/yr (h_{71}^3) at $z = 0.16$, which is about 1/1000th of the core-collapse rate at this redshift. Prajs et al. (2017) measure a rate that is roughly twice as high at $z = 1.13$, and Cooke et al. (2012) estimate that the rate is higher by at least another factor of 5 at $2 < z < 4$. Given our current understanding that SLSNe originate with the deaths of very massive stars typically in low-metallicity environments, such an increase in rate with redshift is to be expected. The precise redshift evolution is of great value to measure as it can either be used to reveal how environmental factors affect the production of SLSNe (and thus help reveal their physical origin), or it can be used to probe how the production of the most massive stars evolves in relation to lower-mass stars (i.e. the SLSN rate evolution may help reveal any changes in the stellar IMF with redshift; Tanaka et al. 2013).

2.1.4. Modelled high-redshift SLSNe rates

Observations show a strong preference for SLSNe toward high star-forming, low-metallicity environments (Lunnan et al. 2014; Leloudas et al. 2015). As such, SLSNe are expected to trace the cosmic star formation history. This is evident from the increase in the observed volumetric rate out to $z \sim 4$ (cosmic star formation peaks at $z \sim 2-3$, see, e.g., Hopkins & Beacom 2006; Moster et al. 2017). The metallicity dependence is likely related to the SLSN production mechanism and dependent on progenitor properties.

To model the comoving SLSN rate as a function of redshift, we combine a star formation rate model ($\dot{\rho}_*$) with a metallicity-dependent efficiency ϵ_Z for their formation, i.e.

$$\dot{n}_{\text{SLSNe}}(z) = \epsilon_Z(z)\dot{\rho}_*(z). \quad (1)$$

This method is based on the rate modelling of GRBs by Trenti et al. (2013). We use DRAGONS’ semi-analytical galaxy-formation model (Mutch et al. 2016), which shows good agreement with both observations and other models. The efficiency function is the key to accounting for different SLSN progenitor models via metallicity. As progenitor models are poorly constrained, we employ the following simple, empirically-motivated prescription. Using the mean stellar metallicity of every galaxy at each simulated redshift, we calculate a SLSN production efficiency factor (using stellar evolution simulations by Yoon et al. 2006) for each galaxy and then average over all galaxies at that redshift. The basic form for the efficiency factor is higher efficiency for lower metallicities with an adjustable lower threshold plateau in place at higher metallicities (as SLSNe may still occur in these environments).

The resulting volumetric rate has been normalised to fit the observed rates of Quimby et al. (2013), Cooke et al. (2012), and more recent analysis by Cooke & Curtin (in preparation). The highest redshift SLSN candidate has been detected by Mould et al. (2017) in deep fields observed with DECam. Their lower limit of 1 deg^{-2} with AB mag < -22.5 requires an order of magnitude correction for SLSNe down to -21.5 (Quimby et al. 2013). This is included in the upper panel of Figure 4 and converted into an observational rate using

$$\dot{N}_{\text{SLSNe}}(z) = \frac{\dot{n}_{\text{SLSNe}}(z) dV}{1+z} \frac{dV}{dz}. \quad (2)$$

The lower panel of Figure 4 shows the integrated SLSN rate beyond redshift z for three models (strong, moderate and no metallicity dependence).

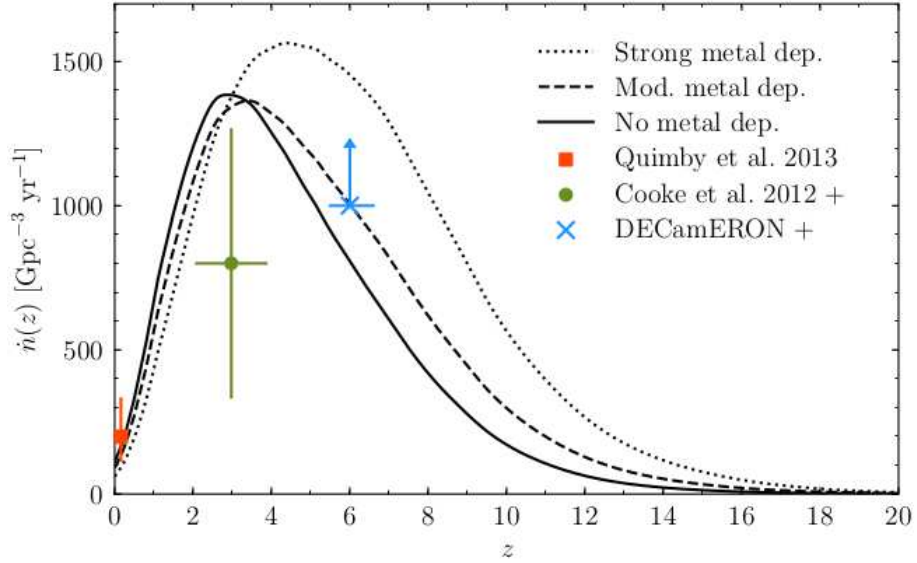
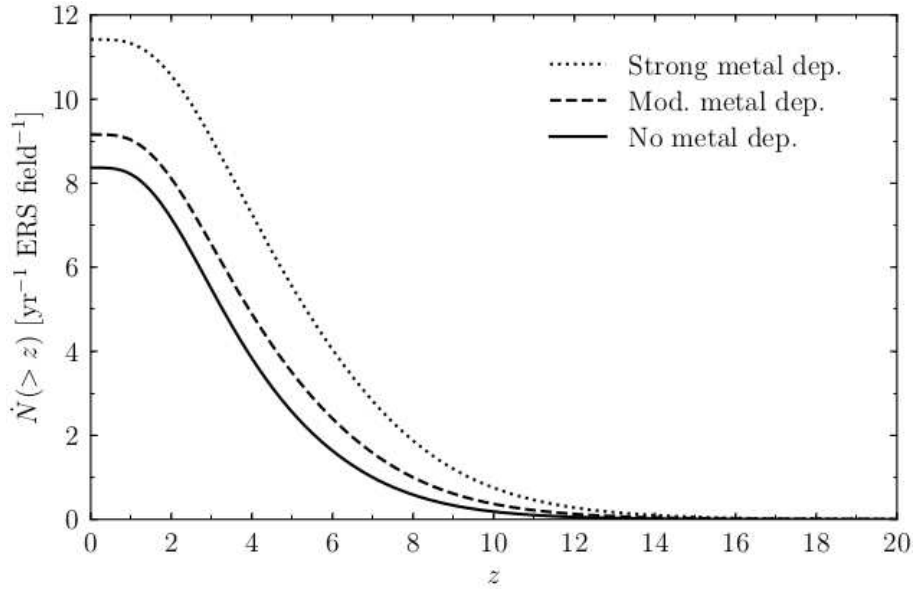


Fig. 4.— Modelled SLSN rates for three progenitor metallicities. Above: Volumetric rates normalised to available observations. Below: Integrated observational rates of SLSNe beyond redshift z .



2.1.5. Normal SNe

“Traditional” supernovae, i.e. core-collapse (Type II and Ib/c) and thermonuclear (Type Ia) explosions, do not reach sufficient peak brightness to be detected at high ($z > 6$) redshifts. They are abundant, however, in the local ($z < 1$) Universe, and therefore will contaminate the *JWST* survey field as the most likely transient sources. Besides the need of filtering out such contaminants from the sample, both CC and Type Ia SNe could be important in probing the star formation rate (SFR) for $z > 1$. To test the detectability of such kind of SNe with *JWST*, we used the various SN spectral templates of Nugent et al. (1997) that extend from $0.1 \mu\text{m}$ to $2.5 \mu\text{m}$ in wavelength. At first the template closest to maximum light was selected in order to get constraints on the detectability from the maximum distance. Figure 5 shows the Nugent Ia template compared to the more recent Hsiao template (Hsiao et al. 2007) tweaked black body that was applied to model the approximate behavior of the SED from the UV to the near-IR. This black body fit was applied during the further calculations.

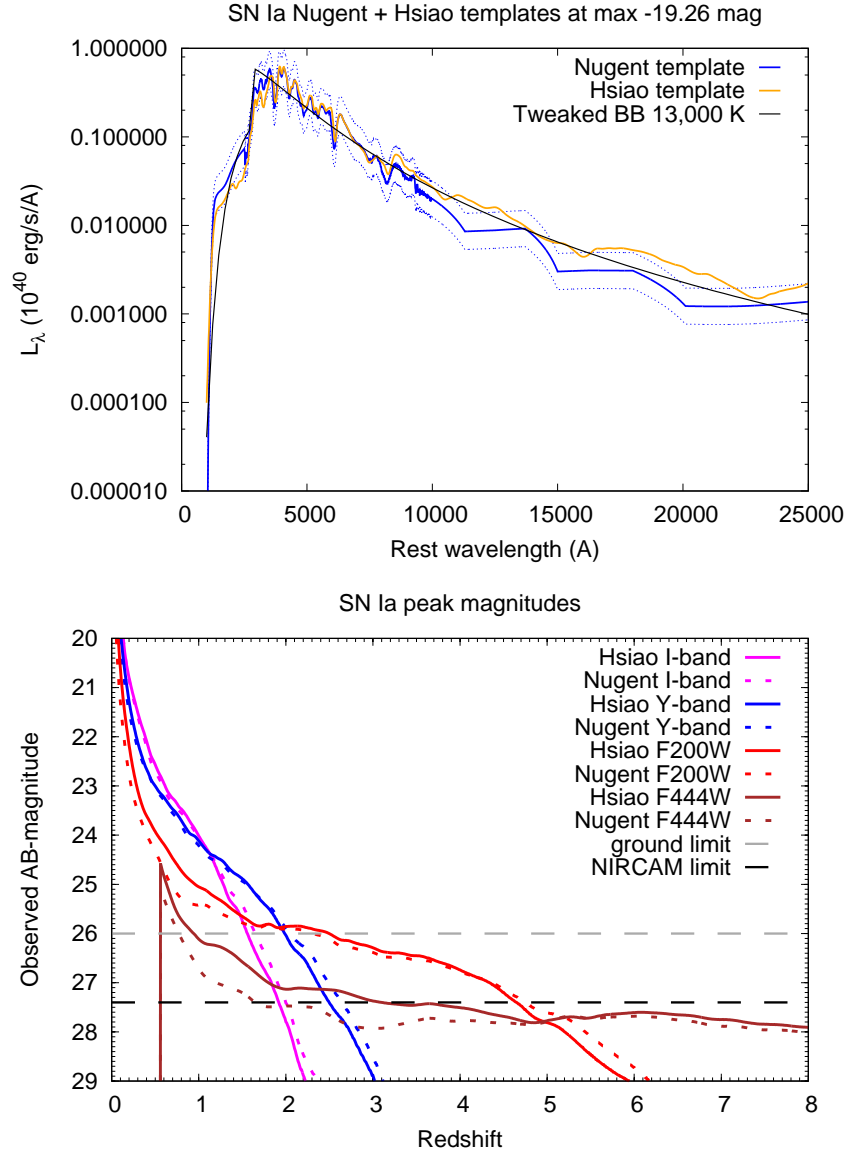


Fig. 5.— Left: the Nugent and Hsiao templates for a fiducial Type Ia SN at maximum with the tweaked black body model (black). Right: the predicted AB magnitudes of Type Ia SNe in various bands as a function of redshift. Dashed horizontal lines indicate the expected sensitivity limit from the ground (grey) and with *JWST* (black).

We adopted the cosmological model from the *Planck* collaboration nicknamed

“Planck13” in `AstroPy` ($H_0 = 67.77$, $\Omega_m = 0.307$, $\Omega_\Lambda = 0.693$) to calculate the luminosity distances in the redshift range of $0 < z < 10$. The peak brightness (in AB magnitudes) as a function of redshift is plotted in the lower panel of Figure 5. It is seen that in the I - and Y -bands SNe Ia cannot be reached from the ground beyond $z \sim 2$, but this limit can be extended up to $z \sim 5$ with *JWST* at 2 and 4.4 μm .

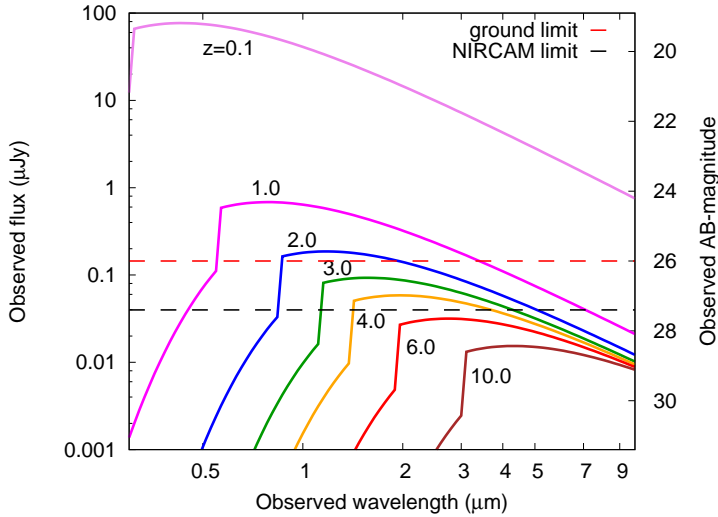


Fig. 6.— The SED of Type Ia SNe at different redshifts (redshifts are color-coded according to the legend). The figure shows the expected flux densities in μJy , while the right panel shows the SEDs expressed in AB magnitudes. The long-dashed horizontal lines illustrate sensitivity limits corresponding to 26 and 27 AB magnitudes.

Figure 6 illustrates which wavelength region of the SED of redshifted Type Ia SNe remains above the detection limits for different redshifts. It is seen that the rest-frame UV/B region of Type Ia SNe redshifted to $z \sim 4 - 5$ are still above the *JWST* detection limit.

These calculations suggest that if a transient (likely a SN) is detected in all 3 bands (1, 2 and 4.4 μm) at appropriate flux levels then it is likely a Type Ia SN within the $0 < z < 2$

redshift range. However, if it is detected at 2 and 4.4 μm but not at 1 μm then it may be a Type Ia SN between $2 < z < 5$. Note that detection at 1 μm is feasible from the ground, so the *JWST* survey should be accompanied by a ground-based survey with a sufficiently large telescope (Subaru or Keck). Such observations are not difficult to schedule because time dilation greatly reduces criticality.

Note also that the presence of Type Ia SNe above $z > 2$ requires the existence of a prompt channel for their progenitors which has negligible delay time after the formation of the carbon-oxygen (C/O) white dwarf. Thus, the *JWST* survey can provide very important constraints on the existence of such a prompt channel.

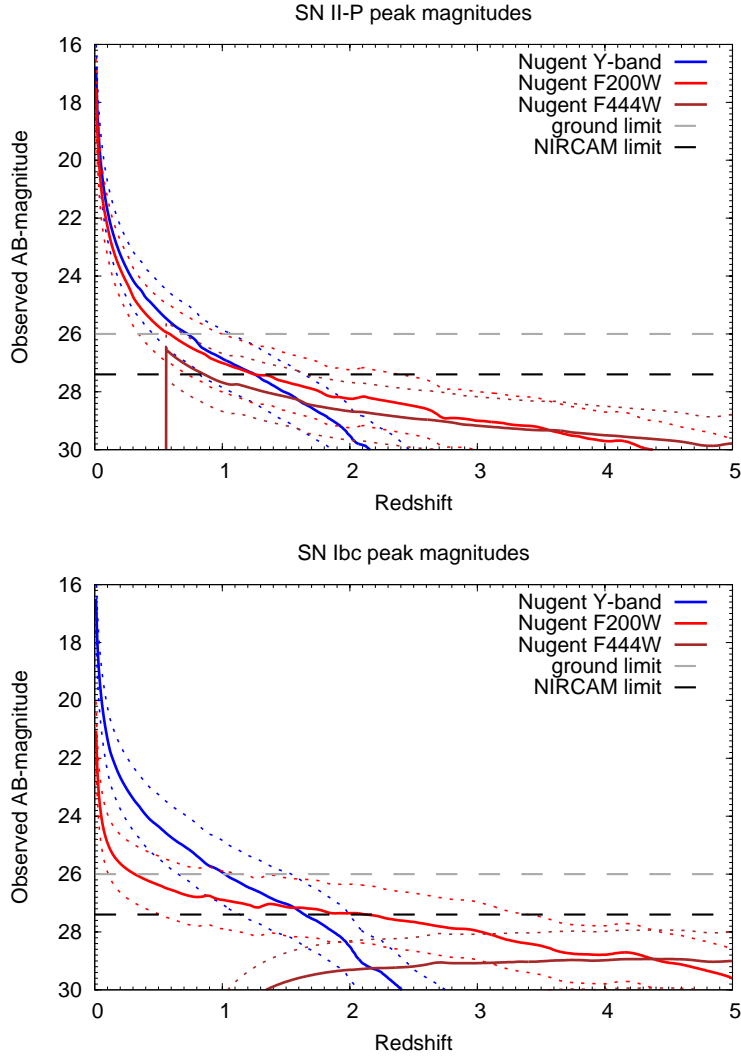


Fig. 7.— Top panel: the range of the expected maximum AB magnitudes of Type II-P SNe from black body fits to the Nugent templates as a function of redshift. The considered photometric bands are color-coded, and the detection limits from the ground and by *JWST* are shown by dashed lines. Lower panel: the same as the top panel but for Type Ib/c SNe.

Traditional core-collapse SNe (Type II and Type Ib/c) tend to have lower peak brightnesses; thus they are expected to show up only at lower redshift above the detection limit of *JWST*. Figure 7 displays their expected peak brightnesses as a function of redshift,

using the Nugent-templates after fitting black bodies to the spectra at maximum. Figure 7 suggests that CC SNe will be detectable with *JWST* only up to $z \sim 2$.

Table 1: A possible classification scheme for low- z SNe based on detections in three bands.

Y(1.03 μm)	F200W	F440W	Classification
+	+	+	Ia $0 < z < 2.5$
+	+	+	II-P $0 < z < 1$
+	+	-	Ibc $z < 1$
-	+	+	Ia $2.5 < z < 5$
-	+	+	II-P $1 < z < 2$
-	+	-	Ibc $1 < z < 3$

Y band is to be obtained from the ground.

Table 1 summarizes a possible classification scheme for the low- z SNe based on detections in three bands: the *Y*-band at 1.03 μm , the *JWST* F200W band around 2 μm and the *JWST* F440W band around 4.4 μm . Plus/minus signs mean detection/nondetection in the given band with fluxes appropriate for a particular SN type.

2.1.6. SN rates

The expected number of SNe within the survey field-of-view (FoV) can be calculated:

$$N = \sum_i R(z_i) \epsilon_i \frac{T}{1+z_i} dV_i(z_i), \quad (3)$$

where z_i is the redshift in the i -th bin, T is the survey time, $R(z_i)$ is the redshift-dependent SN rate per unit volume, dV_i is the differential comoving volume of the i -th redshift bin and ϵ_i is the survey detection efficiency at redshift z_i . The SN rate, $R(z)$, can be expressed as:

$$R(z) = \int SFH(t(z) - \tau) \cdot DTD(\tau) d\tau, \quad (4)$$

where $t(z)$ is the cosmic time at redshift z , $SFH(t)$ is the cosmic star-formation history at redshift z , while $DTD(t)$ is the delay-time distribution for the given SN type. The latter was assumed as a delta function for CC SNe, meaning that there is no significant time delay between the massive star formation and the following SN explosion. This assumption results in $R(z) = SFH(t(z))$.

The rate of Type Ia SN at high redshifts ($z > 2$) is more uncertain. Current models for Type Ia progenitors, either the single degenerate or double degenerate scenario (Iben & Tutukov 1984), predict a strongly decreasing Type Ia rate above $z \sim 2$. There could be, however, a prompt Type Ia population which might explode very shortly after the formation of the white dwarf (WD). As a first approximation, we assumed that the rate of Type Ia SN can be smoothly extended to $z > 2$ from lower redshifts, following the cosmic star-formation history function. This approximation gives only a strongly overestimated upper limit for the expected number of Type Ia SNe at high redshifts. The detected number of such SNe, if any, will be smaller. We applied the empirical formula by Hopkins & Beacom (2006) to estimate the $SFH(z)$ function at different redshifts. Values for the absolute SN rates of the particular types were collected from Bazin et al. (2009), while the fractions of Types II and Ibc within the CC SNe were adopted from Shivvers et al. (2017), being 0.7/0.3. Figure 8 shows the adopted SN rates for each type.

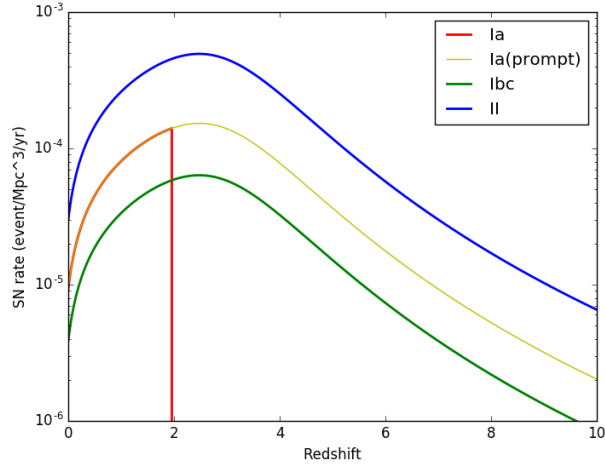


Fig. 8.— The assumed rates for each SN type as a function of redshift.

Finally, the number of SNe within the survey FoV was calculated from Eq. 3 for each type. We adopted $T = 100$ days for the total survey time and the following detection limits in the three bands: Y (from ground): 26 AB mag; $F200W$ ($JWST$): 27 AB mag; $F440W$ ($JWST$): 27 AB mag. Assuming 100% survey efficiency ($\epsilon_i = 1$) as a first approximation, the results are collected in Table 2.

Table 2: The expected number of SNe of various types in the survey FoV during the survey time

SN type	M_{peak} (V)	N (Y)	N (F200W)	N (F440W)
Ia (w/o prompt)	−19.3	19	19	13
Ia (w prompt)	−19.3	23	45	13
Ibc	−17.6	5	6	0
II	−16.8	4	16	4

100% detection efficiency assumed.

In total, we can expect ~ 45 Type Ia, ~ 16 Type II and ~ 6 Type Ibc SNe to be

detectable in the survey field. The number for Type Ia SNe is an upper limit, as it contains the overestimated fraction of the prompt Type Ia SNe. Without the prompt population, the expected number of Type Ia SNe reduces to 19.

2.1.7. *Finding the First Type Ia SNe*

The survey we propose will be able to discover thermonuclear supernovae to a redshift approaching $z \sim 4$. Although the sparse light curve sampling from our survey may not allow us to accurately extract the light curve shapes and derive precise cosmological distances to these SNe, they are nonetheless important in constraining the progenitor systems of Type Ia SNe and test the evolution of their intrinsic magnitudes. Type Ia SNe at such redshifts will experience time dilation by a factor of 4–5. Once discovered, they are expected to be visible by *JWST* for about 6 months, and bright enough for photometric and spectroscopic followup. They can be studied by separate programs aiming to directly measure cosmic deceleration at those redshifts, the ISM towards these SNe, and stellar evolution at very high redshifts. Because we will also discover ~ 50 Type Ia SNe at redshifts around $z \sim 2$, our program will serve as target feeder to programs aiming to measure precision cosmological parameters.

2.2. Large Scale Structure in the Epoch of Reionization

An important question in the epoch of reionization (EoR) is, can a change in the power spectrum of the spatial distribution of galaxies be detected between $z = 6$ –10? We consider whether this is possible in a 0.1 square degree FLARE field. A typical distribution of galaxies in the light cone between $6 < z < 10$ can be created using the Theoretical

Astrophysical Observatory³ (TAO; Bernyk et al. 2016) and the Millennium simulation (Harker et al. 2006, plus SAGE semianalytics; Croton et al. 2016). The brightest galaxies are shown in Figure 9. The luminosity function is shown in Figure 10.

³<https://tao.asvo.org.au>

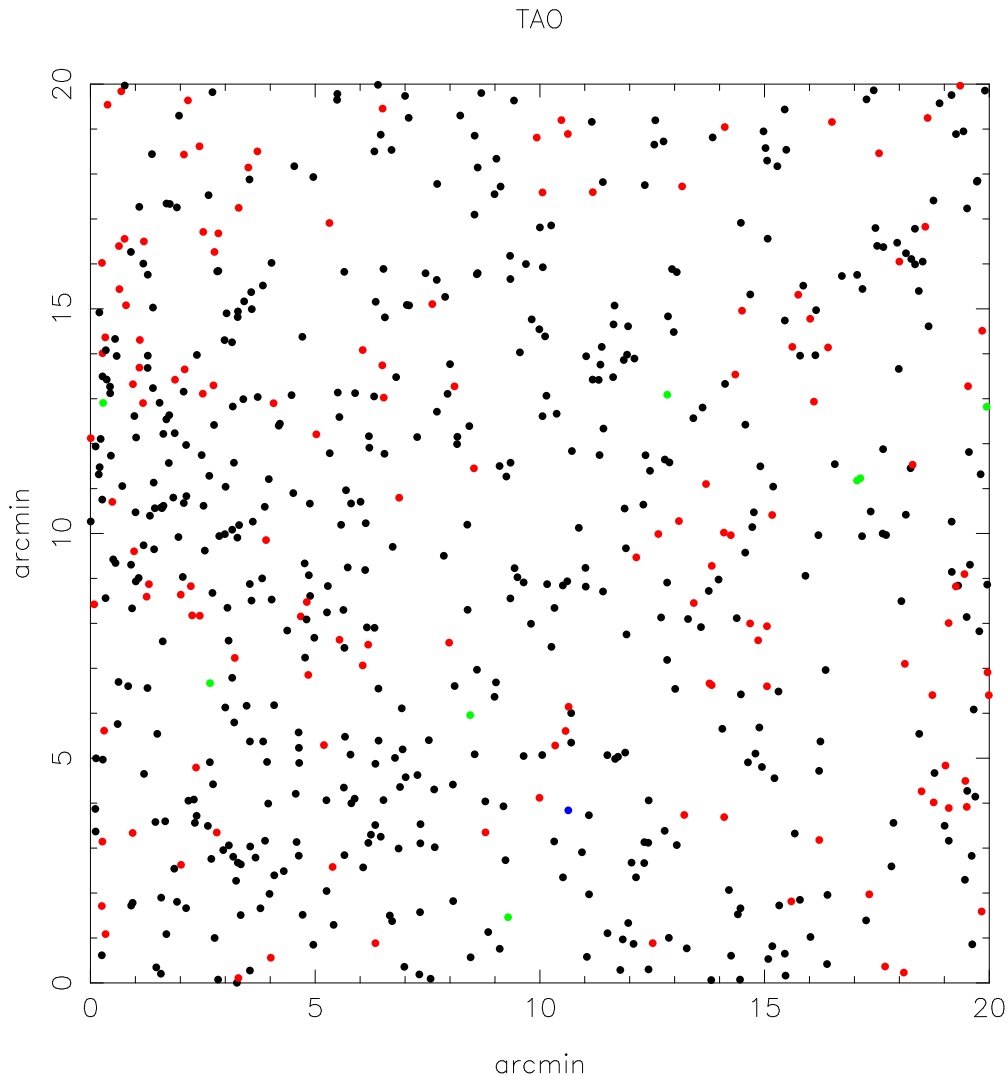


Fig. 9.— Brightest galaxies in a light cone made with TAO in a 400 square arcminute field. Black points have $z = 6$; red points $z = 7$ to blue $z = 9$; One comoving Mpc is ≈ 3 arcminute at $z = 6.56$. The higher density of galaxies in the centre left of the field will yield the largest intensity of ionizing radiation and thus blow a bubble in the neutral hydrogen gas, as seen in the DRAGONS simulations.

The number of galaxies is made to equal the predictions of the DRAGONS simulation Mutch et al. (2016).

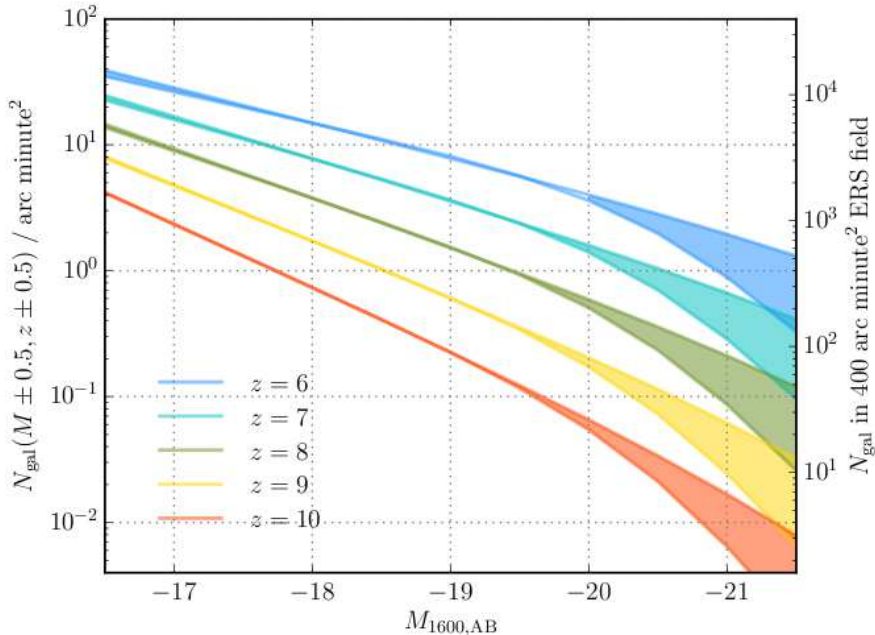


Fig. 10.— The number of galaxies are bound at each redshift by the intrinsic UV luminosity function (upper curve of the shaded envelope) and the dust-corrected UV luminosity function (lower curve of the envelope). Dust is exaggerated at $z = 9$ – 10 . Integrated in $dz = 1$ and $dM = 1$ bins centered over z and M_{UV} ($M_{1600,AB}$).

2.3. Growing supermassive black holes before Reionization

The first SMBH seeds⁴ formed when the Universe was younger than ~ 500 Myr and played an important role in the growth of early ($z \sim 7$) SMBHs (e.g. Pacucci et al. 2015; Natarajan et al. 2017). Much progress has been made in recent years in understanding their formation, growth and observational signatures, but many questions remain unanswered and we are yet to detect these sources. Natarajan et al. (2017) predicted the observational properties and *JWST* detectability of black hole seeds, formed by the direct collapse

⁴Meaning BH beyond stellar mass

of high-redshift halos (e.g. Bromm & Loeb 2003a, or as remnants of Pop III stars, e.g. Volonteri & Rees 2005).

When primordial, atomic-cooling halos ($T_{\text{vir}} > 10^4 \text{ K}$) are exposed to a high-intensity Lyman-Werner flux, $J_\nu > J_\nu^\bullet$ (Loeb & Rasio 1994; Lodato & Natarajan 2006; Shang et al. 2010) the destruction of H_2 molecules allows a rapid, isothermal collapse. The precise value of J_ν^\bullet depends on several factors, but there is a general consensus that it should fall in the range $30 < J_{21}^\bullet < 1000$, depending on the spectrum of the sources (Sugimura et al. 2014). Several theoretical works (Bromm & Loeb 2003b; Begelman et al. 2006; Volonteri et al. 2008; Shang et al. 2010; Johnson et al. 2012) have shown that the result of this collapse is the formation of a direct collapse black hole (DCBH) of mass $M_\bullet \approx 10^{4-6} M_\odot$ (Woods et al. 2017; Umeda et al. 2016)).

Guided by theoretical estimates in Pacucci et al. (2015) and Natarajan et al. (2017), these sources are predicted to be particularly bright in the infrared. In the near infrared, these sources should be significantly brighter than 28th magnitude (26 on average, depending on the initial BH mass and on the physical properties of the host halo), while Pop III seeds are characterized by infrared magnitudes above 29 on average and they could be unobservable with the *JWST*. Pacucci et al. (2016) (see also Pallottini et al. 2015; Pacucci et al. 2017) claimed the possibility of two $z \gtrsim 6$ DCBH candidates in a survey such as CANDELS/GOODS-S (Illingworth et al. 2016) with a significant X-ray emission. DCBHs are thus high-value targets for the *JWST* in the infrared. In what follows we present a general overview on the properties and detectability of DCBHs.

2.3.1. *The brightness, number density and detectability of DCBHs*

Assuming that a DCBH is accreting at the Eddington rate and that it is Compton-thick (Yue et al. 2013) ($N_{\text{H}} \gtrsim 10^{24} \text{ cm}^{-2}$, where N_{H} is the column number density of the host galaxy), then its $4.5 \mu\text{m}$ apparent magnitude is a simple function of black hole mass. The computation is performed for an object located at $z \sim 13$, i.e. well inside the cosmological period during which the formation of DCBHs is more likely (Yue et al. 2013). A DCBH seed is predicted to have a mass in the range $\sim 10^4\text{--}10^6 M_{\odot}$ (Ferrara et al. 2014). When it grows to $\gtrsim 2 \times 10^6 M_{\odot}$, it becomes detectable in the survey that we are proposing (i.e. brighter than 26.5 mag at $4.5 \mu\text{m}$). A DCBH could, however, be characterized by super-Eddington accretion rates (Pacucci et al. 2015). In this case the relation between mass and brightness is less straightforward to predict, and a DCBH could be detectable even for masses $\lesssim 2 \times 10^6 M_{\odot}$.

In the literature, the predicted number density of DCBHs widely varies, from $\sim 10^{-10}\text{--}10^{-1} \text{ Mpc}^{-3}$ at $z \sim 10$ (comoving units). The large span in the predictions is mainly due to the uncertainties on the critical external field strength that can fully suppress the H_2 formation, the clustering of the potential DCBH formation sites, and the feedback effects. A summary of the DCBH number densities predicted by different papers is shown in Figure 11 (taken from Habouzit et al. 2016). While the detailed description of each model is found in the caption of the original paper, here we just want to show the great variety of predictions. The number density could be even as high as $\sim 0.1 \text{ Mpc}^{-3}$ at $z \sim 13$, due to our condition of producing the observed cosmic near-infrared background fluctuations levels (Yue et al. 2013) from these sources.

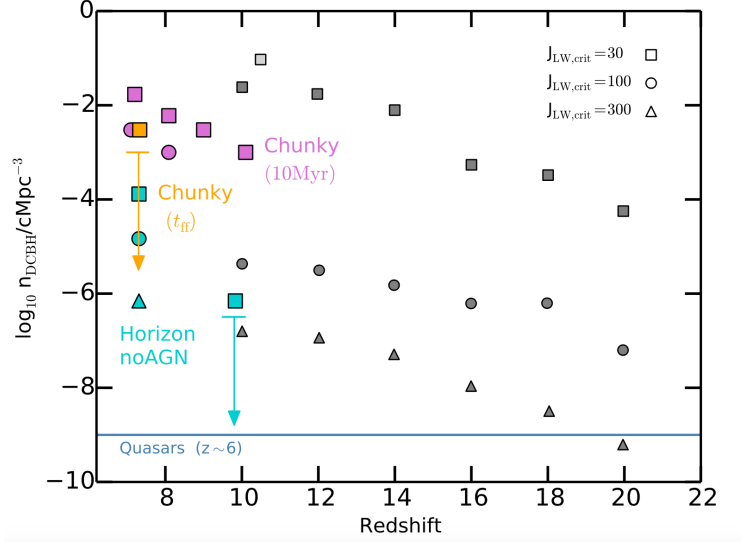


Fig. 11.— The number density of DCBHs predicted by several works . The figure is adapted from Habouzit et al. (2016). While the detailed description of each model is found in the caption of the original paper (and tabulated below), here we only choose to show the great variety of predictions.

Table 3: Symbols and models.

Symbols	n_{DCBH} Model	M_{\bullet}^*	N_{H}
stars	Y13	–	$1.2 \times 10^{25} \text{ cm}^{-2}$
filled circles	A12, $J_{\text{LW}}^c = 30$	$10^6 M_{\odot}$	10^{25} cm^{-2}
open circles	D14, $J_{\text{LW}}^c = 30$	$10^6 M_{\odot}$	10^{25} cm^{-2}
filled squares	A12, $J_{\text{LW}}^c = 30$	$5 \times 10^5 M_{\odot}$	10^{25} cm^{-2}
open squares	D14, $J_{\text{LW}}^c = 30$	$5 \times 10^5 M_{\odot}$	10^{25} cm^{-2}
filled triangles	A12, $J_{\text{LW}}^c = 30$	$10^6 M_{\odot}$	10^{20} cm^{-2}
open triangles	D14, $J_{\text{LW}}^c = 30$	$10^6 M_{\odot}$	10^{20} cm^{-2}

Regarding the detectability, we convert the number density to a surface number

density of DCBHs brighter than some threshold magnitude by specifying a mass function. Notwithstanding large uncertainties in the DCBH mass function, we can assume a Schechter formula or a bimodal Gaussian distribution (Ferrara et al. 2014). In Figure 12 we show the surface number density of DCBHs brighter than 26.5 mag at $4.5 \mu\text{m}$, for the DCBH number density predicted in Agarwal et al. (2012) (A12), Yue et al. (2013) (Y13) and Dijkstra et al. (2014) (D14) for various DCBH and mass function parameters (see Table 3). Basically, Compton-thick DCBHs are more detectable because more energy is re-processed to the rest-frame UV/optical band, then redshifted to the near-infrared band.

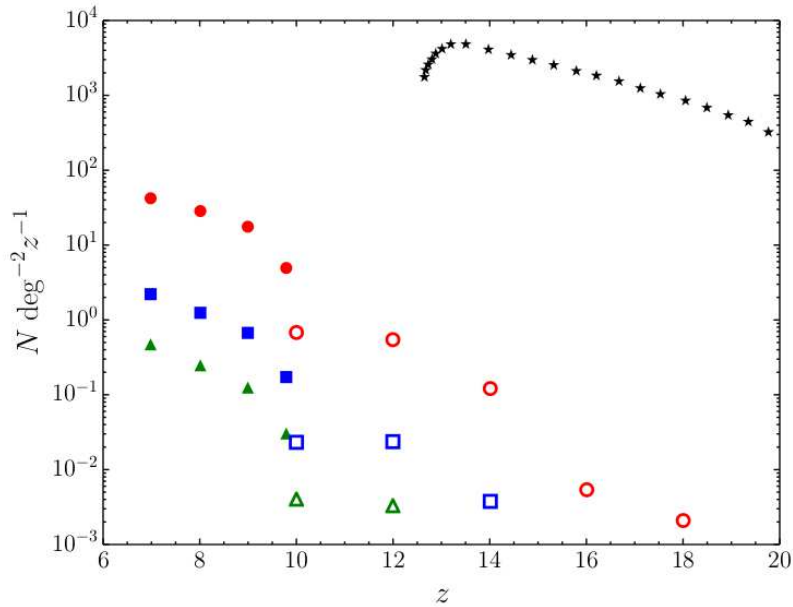


Fig. 12.— The surface number density of DCBHs brighter than 26.5 mag at $4.5 \mu\text{m}$ in various models. We show the surface number densities predicted in Agarwal et al. (2012), Yue et al. (2013) and Dijkstra et al. (2014) for various DCBH and mass function parameters.

2.3.2. *The infrared colors of DCBHs*

According to Pacucci et al. (2016), a DCBH has infrared colors significantly different from the typical QSO or star-forming galaxy. For the photometric filters of our interest, Y ($1 \mu\text{m}$), $2.2 \mu\text{m}$ and $4.4 \mu\text{m}$, we predict photometric colors $Y - 2.2$ and $2.2 - 4.4$ larger than 2. DCBH candidates can be preselected even in purely photometric surveys.

Spectroscopic signatures of DCBHs are: (i) strong HeII 1640 \AA emission line, (ii) strong Ly α emission (but if the DCBH is extremely Compton-thick, the Ly α emission would be trapped and converted into continuum emission), (iii) absence of metal lines. Candidates could also be selected according to their photometric colors (Figure 11) (Pacucci et al. 2016).

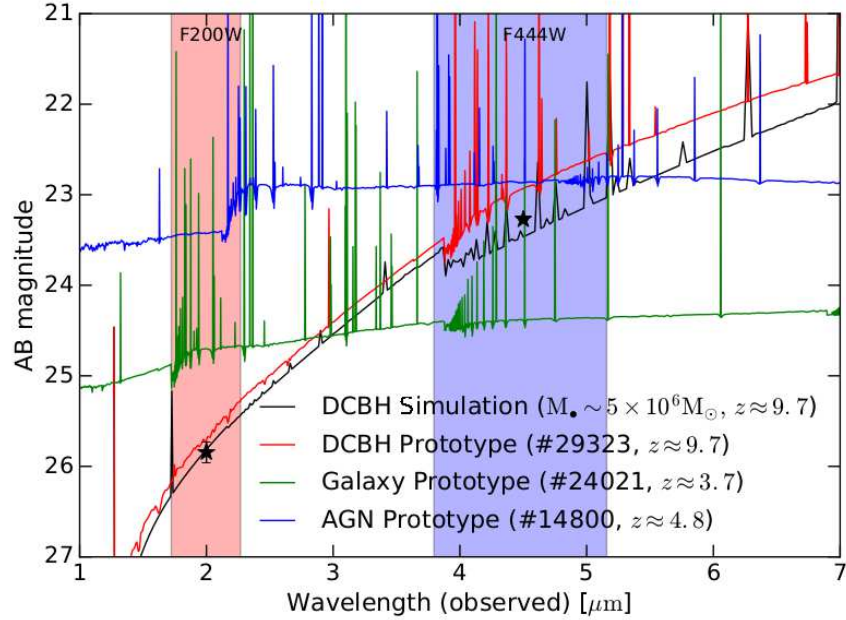


Fig. 13.— Comparison between the stellar SEDs of three GOODS-S objects with the computed SED of a $5 \times 10^6 M_{\odot}$ black hole, born out of a DCBH with initial mass around $10^5 M_{\odot}$. NIRCAM photometric bands are shaded. Stars (numerical simulations) show the magnitude error bars. Objects 29323 and 14800 have X-ray counterparts (i.e. they are likely associated with a black hole), while 24021 does not (i.e. it is likely a normal galaxy). Moreover, object 29323 is characterized by very negative colors (i.e. its infrared SED is very steep, as we predict for DCBHs), while objects 14800 and 24021 are not. The steepness of the SED and the infrared magnitudes for the object 29323 are well fitted by the spectrum predicted for a $\sim 5 \times 10^6 M_{\odot}$ black hole. In the computed SED for a DCBH, the He II line ($0.164 \mu\text{m}$ rest-frame) is visible and it is marginally inside the H band at $z \sim 9.7$.

Although TDEs around DCBHs produce spectacular transients that are well within the sensitivity of our proposed survey, fluctuations in normal accretion onto the DCBH also drive variations in near-infrared (NIR) luminosities that could be detected as well. These variations are due to disruptions in flows onto the DCBH over a large range of

spatial scales and times. New radiation hydrodynamical simulations of DCBH growth in cosmological environments show that fluctuations in cold flows into the host galaxy on kpc scales can lead to large variations in BH luminosity on timescales of Myr, as shown in Figure 14 (Smidt et al. 2017). But brightening and dimming could occur on times as short as the light-crossing time of the BH. Numerical simulations that achieve sub-AU resolution show that catastrophic baryon collapse in atomically-cooled halos leads to the formation of bursty accretion disks around supermassive primordial protostars, the precursors to DCBHs (Becerra et al. 2015). Clumpy accretion due to turbulence in the disk can result in changes in luminosity of about an order of magnitude on timescales of days or weeks in the rest frame of the nascent DCBH. Such variations should be easily detectable by our proposed survey.

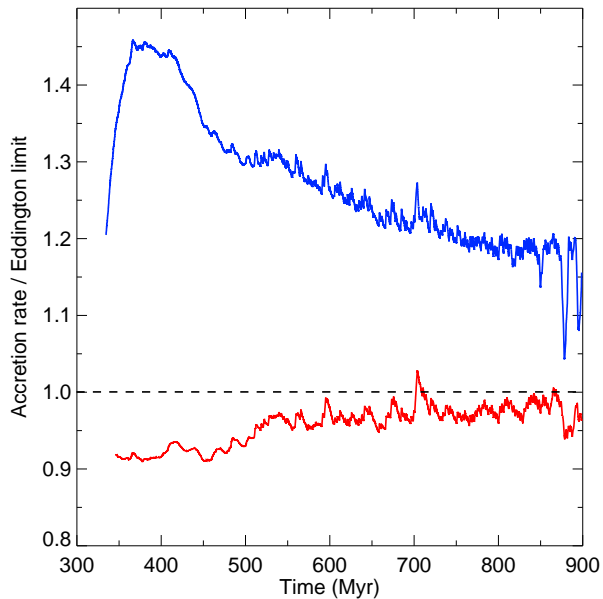


Fig. 14.— DCBH accretion rates as a fraction of the Eddington limit. Blue: no X-ray feedback. Red: with X-ray feedback from the BH.

According to Kashiyama & Inayoshi (2016), the TDE rate is ~ 10 per DCBH within

~ 1 Myr at the DCBH early growth stage. If the TDE only happens at the early stage, and assuming that the typical lifetime of a DCBH is ~ 50 Myr, then we expect the TDE rate to be $\sim 2 \times 10^{-7} \text{ yr}^{-1}$ per DCBH. Multiplying the surface number density of a steady accreting DCBH (Figure 12) by this rate, we obtain the detectability of TDEs: $\sim 10^{-2} \text{ deg}^{-2} z^{-1} \text{ yr}^{-1}$ at maximum at $z \sim 13$ in Y13, and $\sim 2 \times 10^{-3} \text{ deg}^{-2} z^{-1} \text{ yr}^{-1}$ at maximum at $z \sim 7$ in A12. However, if the TDE happens through the whole lifetime of a DCBH, then we expect a rate as high as $\sim 0.5 \text{ deg}^{-2} z^{-1} \text{ yr}^{-1}$ in Y13. This value, while obviously lower when compared to the rate of TDEs for all SMBHs, is a serious consideration for the present survey. A signature of TDEs is order of magnitude flares in rise times of $(1 + z)$ times 30 days.

2.4. Serendipitous high-redshift transients

2.4.1. Kilonovae

The tidal disruption of a neutron star in a binary companion with either another neutron star or a black hole has long been of astrophysical interest, since it has long been understood that the decompression of neutron star material could be a site for r-process nucleosynthesis (Lattimer & Schramm 1974; Lattimer et al. 1977; Symbalisty & Schramm 1982). Interest was further heightened when it was realized that the same systems could provide an electromagnetic counterpart for gravitational wave signals (Li & Paczyński 1998; Kulkarni 2005; Metzger et al. 2010). These systems have been dubbed kilonovae or macronovae, but we will use the former name. For an excellent review of the entire field, see Metzger (2017). The expected electromagnetic signatures are illustrated in Figure 15.

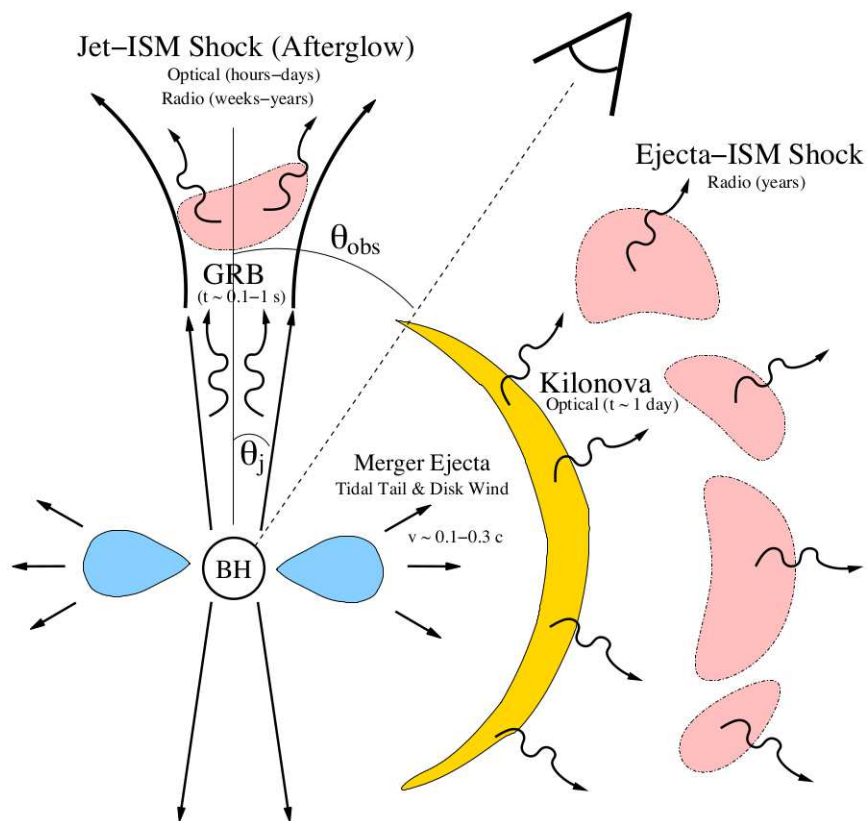


Fig. 15.— The basic picture of the various electromagnetic signatures produced in a merging neutron star event. The kilonova emission comes from the semi-symmetric ejecta (from Metzger & Berger 2012).

Population synthesis models predict gravity wave detection rates of NS–NS/BH–NS mergers of $\sim 0.2-300$ per year, for the full design sensitivities of Advanced LIGO/Virgo (Abadie et al. 2010; Dominik et al. 2015). Empirical estimates predict ~ 8 NS–NS mergers per year in the Galaxy (Kalogera et al. 2004a,b; Kim et al. 2015). Numerical models of the event rate estimate $\sim 1000 \text{ Gpc}^{-3}\text{yr}^{-1}$ (Tanaka 2016) with a spectrum shown in Figure 16.

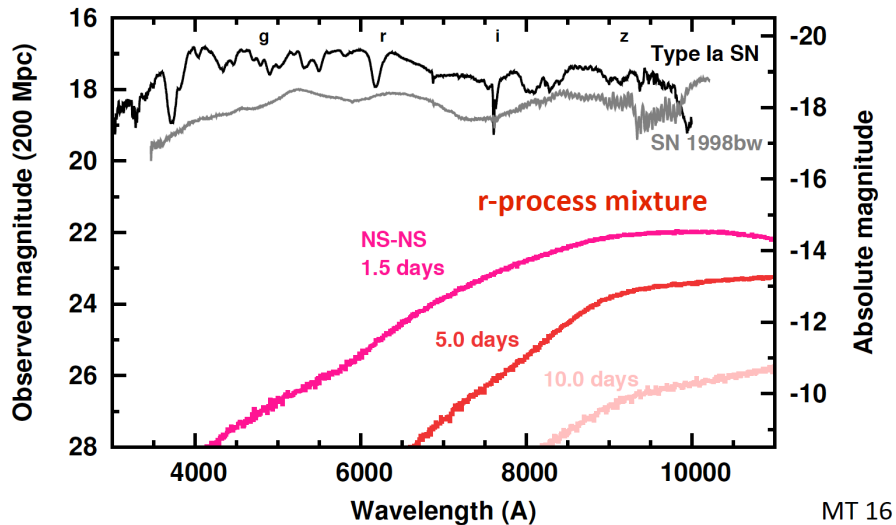


Fig. 16.— The spectrum of the relativistic ejecta of a NS–NS merger compared with that of supernovae (from Tanaka 2016).

Models of the disk-wind structure have been performed by Kasen et al. (2015) and the dynamics and nucleosynthesis of BH–NS mergers have been studied by Fernández et al. (2017) and Metzger (2017) and references therein.

We have begun preliminary modeling with the generalized stellar atmospheres code PHOENIX (P. Vallely & E. Baron, in preparation). We include some r-process elements in full NLTE, and the time is right to begin NLTE modeling as the atomic data to construct the model atoms for all r-process elements is now available (Fontes et al. 2017).

Several kilonovae should be visible in our proposed program and understanding these events is important for understanding the site of the r-process as well as crucial to providing electromagnetic counterparts to gravitational wave events.

2.4.2. Formation of globular clusters

Renzini (2017) suggests that a proto globular cluster in the EoR reaches AB = 28 mag for a Myr. At low metallicity these objects are candidates to produce SLSNe with $25 < AB < 28$. If 5% of the cosmic SFR from $z = 9$ to 6 were in globular clusters (GCs), we would have $2 \times 10^5 M_{\odot} \text{Mpc}^{-3}$. For $M/L = 10^{-2}$ that is $2 \times 10^7 L_{\odot} \text{Mpc}^{-3}$. In 1 square degree, $dn/dt \sim 1$ GC SLSN per year.

Globular clusters are laboratories for SNe. Since IMFs $\propto m^{-2}$, some half of the mass terminates in SNe. The kinetic energy of a $10^6 M_{\odot}$ GC is $10^6 \times 10^{12} \times 10^{33} = 1$ foe. Depositing 1 foe in it from a SLSN will come close to unbinding the cluster. According to chemical evolution theory removing the gas from the cluster is *required* to retain the observed low metallicity, and a SLSN may well be the agent⁵.

3. The FLARE *JWST* Transient Field

Now we need to detail the methodology for an efficient *First Transients* survey. We propose to survey the North Ecliptic Pole (NEP) in two colors down to 27.4 mag (AB). This is very much deeper than the *JWST* Time-Domain Community Field (Jansen et al. 2017). The NIRCAM with filters F200W and F444W is most appropriate to the project. We will also employ NIRISS for deeper coverage in the F444W band for a small fraction of the field in the parallel mode. For an Early Release Science time-domain survey, two visits of the NEP field would be made at two epochs separated by 91.3 days. For these purposes the primary survey instrument is NIRCAM, with NIRISS in parallel mode. The survey employs two filters, F200W and F444W with NIRCAM and F444 only with NIRISS. Medium background level is appropriate. The detector is to be set up to read out the full array, and

⁵See also Recchi et al. (2017), Boylan-Kolchin (2017) .

the readout pattern is SHALLOW4; the observations employ 3 Groups, 2 Integrations, and 1 Exposures, in accordance with STScI Exposure Time Calculator tools. This gives a total exposure time of 322.1 s for each pointing and a S/N ratio of 3.1 and 3.2 in F200W and F444W, for targets of 27.4 mag (AB) and 27.5 mag (AB), and a S/N ratio of 5.0 in F200W and F444W, for targets of 26.9 mag (AB) and 27.0 mag (AB), respectively. For efficient telescope steering, we foresee observations grouped into a 9×5 rectangular mosaic. Full dithering is important in rejecting spurious signals but carries a prohibitively expensive overhead for a wide field survey. However, in our simulations of *JWST* observations, we found that sub-pixel dithering with 2-POINT-MEDIUM-WITHNIRISS is sufficient for rejecting spurious signals due to hot pixels and cosmic rays. For a fully successful program, one should expect to revisit the same field multiple times, which will help build up more robust templates and aid in rejecting cosmic rays.

3.1. Why cluster lensing does not help find more transients

As pointed out in Sullivan et al. (2000) there are three important effects one has to consider in understanding any gain (or loss) in the SN detection rate via a lensing cluster. These are: the area-weighted lensing magnification, the SN rate as a function of redshift and the limiting magnitude of the survey. As can be seen in their Figure 3 and Table 1 for a simulated HST survey, modest gains can be had for $1.5 < z < 2.0$ due to the fact that the intrinsic rates are flat or slowly declining at these redshifts and amplification brings SNe at the lower end of the luminosity function into the realm of detection. Interestingly, the SN detection efficiency *drops* for $z < 1.5$ as the area surveyed behind a cluster shrinks in proportion to the amplification factor. Since HST can easily discover SNe without magnification below these redshifts, by reducing the survey area one suffers a net loss.

This fact is exacerbated in any survey by *JWST* to depths of AB = 27 mag. Since the

SN rate starts dropping dramatically beyond a redshift of 2–3 (driven by the $1 + z$ time dilation factor; see Figure 2 of Sullivan et al. 2000) and *JWST* is already sensitive to even the lowest end of the luminosity function for Type Ia SNe at these redshifts (and more than 70% of the CC SNe), a lensing cluster search provides no net benefit. In fact, there would be appreciable loss due to the drop in effective area.

3.2. Probabilistic Target Classification

With our choice of filters, we are able to make a preliminary screening by the variability of the sources and their location on the color–magnitude diagram. Figure 17 shows as an example how different objects may be classified. It is clear from the figure that DCBH stand out clearly as extremely red objects, whereas SLSNe and Type Ia SNe fall on distinct areas on the color–magnitude diagram.

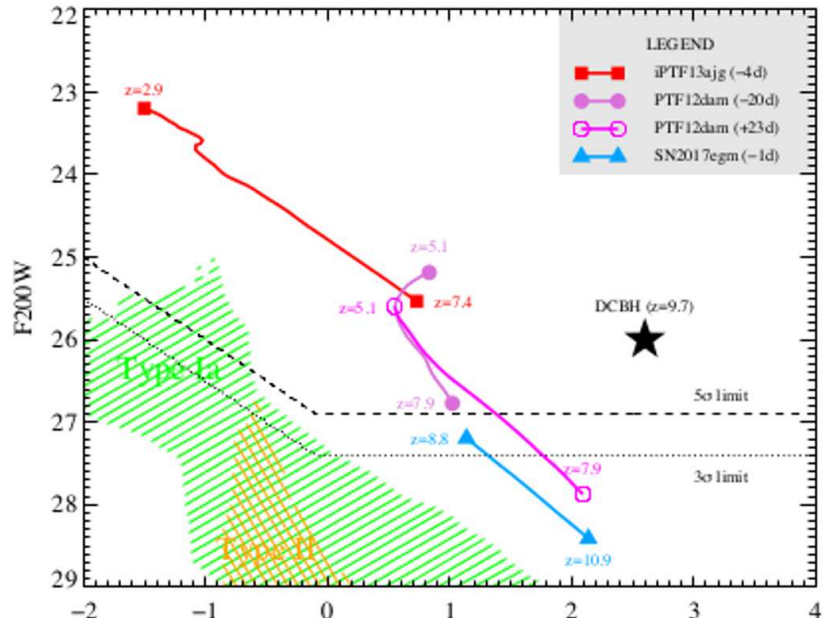


Fig. 17.— The color–magnitude diagram of Type Ia SN, SLSNe, and DCBH at various redshifts. The numbers show the redshifts of the targets.

Ambiguities are inevitable and more data will be needed. We plan to acquire deep images in *grizY* bands from the ground to supplement the *JWST* data. This will be helpful in eliminating brown dwarfs, whose lack of variability at K band (Khandrika et al. 2013) escapes triggering our survey. We remark that at the redshift of interest, SLSNe are most likely to be much brighter than their host galaxies and may actually appear “hostless”. This applies also to DCBHs.

3.2.1. Brown dwarfs

These objects are redder than brown dwarfs, as can be seen from Figures 18 and 19 calculated by Simpson and Baron using models of Barman et al. (in preparation).

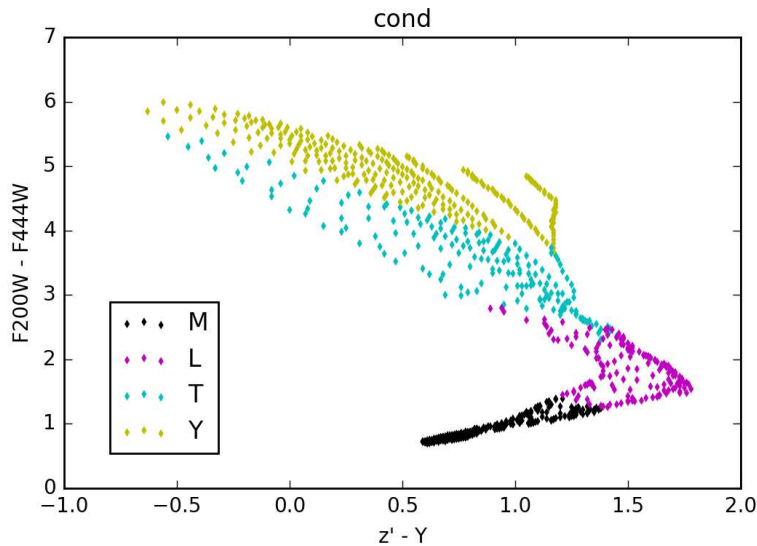


Fig. 18.— Colors of brown dwarfs of types M, L, T, Y.

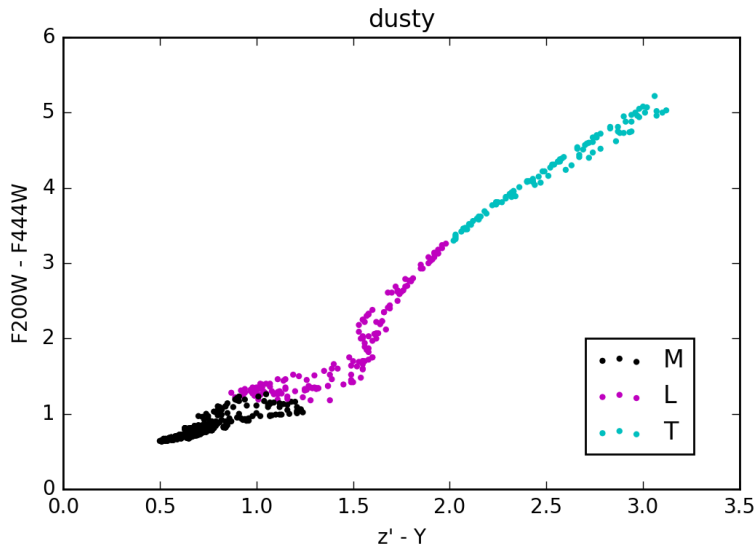


Fig. 19.— Colors of brown dwarfs with dusty atmospheres.

4. Facilitating First Transients discovery

The vision of the *JWST* is to discover the first stars to appear in the Universe. For this to be accomplished in fact with this facility we must see not their faint birth but their bright SNe. The FLARE project would lay the foundation to do this over the life of the *JWST* mission by creating a James Webb Transient Factory (JWTF), in which all the mission’s repeat imaging data would be analysed for transients.

4.1. The design of the FLARE project

4.1.1. Observations and deliverables with JWST

Our observing plan is tailored to deliver some transients from the EoR over the first six months, both single supernovae and transients resulting from the formation by redshift

6 of SMBHs. But according to §2 the highest redshift supernovae are rare enough that only operation of a JWTF for five years will find them.

Appropriate deliverables will therefore include the software for a JWTF, developed at the Weizmann and the Mitchell Institutes, which could be operated at Space Telescope Science Institute, and also, through a collaboration with Swinburne University and drawing on the Millennium Simulation and other similar databases, a module of TAO which will allow full simulation of all GO proposals for imaging with *JWST* by the proposers themselves in the course of preparing Cycle 2 and later cycles.

TAO houses data from popular cosmological N -body simulations and galaxy formation models, primarily focused on survey science. Mock catalogues can be built from the database without the need for any coding. Results can be funneled through higher-level modules to generate SEDs, build custom light-cones and images.

TAO will be expanded to include more detailed modelling of the galaxies and SNe at high redshift relevant to the *JWST*, and new tools to produce mock observations that mimic those that JWTF will process. This will allow predictions to be made using the advanced simulations that TAO hosts and interpretation of the results as they arrive.

4.1.2. Supporting observations and followup strategies

To realise its full potential, time domain astronomy makes serious demands on cadence, followup, and multiwavelength coverage. High-redshift investigations are less demanding than local ones due to time dilation, and we anticipate that NEP revisits can be proposed with normal STScI planned annual cycles. Spectroscopic followup of targets of opportunity with NIRSpec and ELT instruments may also be a modest imposition on these facilities. Deep ground based reference fields at shorter wavelengths, however, should be initiated

immediately for the purpose of eliminating foreground objects. The Subaru Strategic Program (Aihara et al. 2017) is a model for such data and adding the NEP to the current set of fields seems to us to be a priority. X-ray followup of *JWST* high-redshift transients will also be vital.

5. Conclusion

The definitive image of the unmistakable structure of the early Universe is the *WMAP* and *Planck* iconic picture (Bennett et al. 2003; Planck Collaboration et al. 2016). The vision of *JWST* is to link this structure and the associated precision cosmology to the first stars formed from the pristine gas out there in protogalactic clumps. Those first stars are individually too faint, and even first galaxies will still be challenging for *JWST*, especially if a representative sample be studied.

In this white paper, we have demonstrated that instead of hammering at still images, observations of transients offer an elegant alternative method of characterizing the early Universe. Information about stellar populations and the IMF is encapsulated in SLSNe, and TDEs (and the intrinsic variability of the accretion flow) can trace the mysterious build-up of billion solar mass SMBHs within few hundreds of millions of years. Detecting and characterizing first SLSNe and TDEs in sufficient numbers are the goals of the FLARE project for *JWST*.

We have shown that monitoring with *JWST* a 0.1 square degree field at 2 and 4 μm and moderate depth can achieve these goals. Ground based deep imaging at shorter wavelengths will complete the inventory of the field and help avoid false alarms.

After this quantitative confirmation at the level of transient categories, we will move on to numerical simulations to determine similarly quantitatively how many events need to

be found and which combinations of time baseline, cadence, colour information, and field size yield the highest success rates in the classification of high-redshift transients. This will deliver a solid justification of the significant investment of telescope time over the life of the mission.

We intend to make immediately public all transients found by the FLARE project. This will enable the community to define and execute follow-up observations of the transients themselves as well as of their environments of which the high-redshift transients represent the tips of their luminosity functions in transparent regions of the early Universe. The $(1 + z)$ -fold time dilation makes the planning of such efforts well feasible. We will develop and offer tools to perform analogous searches for transients in all other *JWST* fields which throughout the lifetime of *JWST* require repeated observations. This will lead to an enlarged homogeneous real-time database of high-redshift transients at no extra cost.

REFERENCES

- Abadie, J., Abbott, B. P., Abbott, R., et al., *Classical and Quantum Gravity*, 27, 173001
- Abel, T., Wise, J. H., & Bryan, G. L., *ApJ*, 659, L87-L90
- Agarwal, B., Johnson, J. L., Khochfar, S., et al., *MNRAS*, 469, 231-236
- Agarwal, B., Johnson, J. L., Zackrisson, E., et al., *MNRAS*, 460, 4003-4010
- Agarwal, B., Khochfar, S., Johnson, J. L., et al., *MNRAS*, 425, 2854-2871
- Aihara, H., Arimoto, N., Armstrong, R., et al., *ArXiv e-prints*, arXiv:1704.05858
- Alvarez, M. A., Bromm, V., & Shapiro, P. R., *ApJ*, 639, 621-632
- Barkana, R., & Loeb, A., *Reports on Progress in Physics*, 70, 627-657
- Barkat, Z., Rakavy, G., & Sack, N., *Physical Review Letters*, 18, 379-381
- Bazin, G., Palanque-Delabrouille, N., Rich, J., et al., *A&A*, 499, 653-660
- Becerra, F., Greif, T. H., Springel, V., & Hernquist, L. E., *MNRAS*, 446, 2380-2393
- Begelman, M. C., Volonteri, M., & Rees, M. J., *MNRAS*, 370, 289-298
- Bennett, C. L., Hill, R. S., Hinshaw, G., et al., *ApJS*, 148, 97-117
- Bernyk, M., Croton, D. J., Tonini, C., et al., *ApJS*, 223, 9
- Bowler, R. A. A., McLure, R. J., Dunlop, J. S., et al., *MNRAS*, 469, 448-458
- Boylan-Kolchin, M., *ArXiv e-prints*, arXiv:1711.00009
- Bromm, V., *Reports on Progress in Physics*, 76, 112901
- Bromm, V., & Loeb, A., *ApJ*, 596, 34-46

—, ApJ, 596, 34-46

—, ApJ, 642, 382-388

Bromm, V., & Yoshida, N., ARA&A, 49, 373-407

Bromm, V., Yoshida, N., Hernquist, L., & McKee, C. F., Nature, 459, 49-54

Bruzual, G., & Charlot, S., MNRAS, 344, 1000-1028

Caplar, N., Lilly, S. J., Trakhtenbrot, B., & PTF Collaboration Active Galactic Nuclei:
What's in a Name?, 60

Chatzopoulos, E., & Wheeler, J. C., ApJ, 748, 42

Chatzopoulos, E., Wheeler, J. C., & Couch, S. M., ApJ, 776, 129

Chen, K.-J., Heger, A., Woosley, S., Almgren, A., & Whalen, D. J., ApJ, 792, 44

Chen, K.-J., Heger, A., Woosley, S., et al., ApJ, 790, 162

Chen, K.-J., Woosley, S., Heger, A., Almgren, A., & Whalen, D. J., ApJ, 792, 28

Cooke, J., Sullivan, M., Gal-Yam, A., et al., Nature, 491, 228-231

Croton, D. J., Stevens, A. R. H., Tonini, C., et al., ApJS, 222, 22

de Barros, S., Vanzella, E., Amorín, R., et al., A&A, 585, A51

De Cia, A., Gal-Yam, A., Rubin, A., et al., ArXiv e-prints, arXiv:1708.01623

de Souza, R. S., Ishida, E. E. O., Johnson, J. L., Whalen, D. J., & Mesinger, A., MNRAS,
436, 1555-1563

de Souza, R. S., Ishida, E. E. O., Whalen, D. J., Johnson, J. L., & Ferrara, A., MNRAS,
442, 1640-1655

- Dijkstra, M., Ferrara, A., & Mesinger, A., MNRAS, 442, 2036-2047
- Dominik, M., Berti, E., O’Shaughnessy, R., et al., ApJ, 806, 263
- Fernández, R., Foucart, F., Kasen, D., et al., Classical and Quantum Gravity, 34, 154001
- Ferrara, A., Salvadori, S., Yue, B., & Schleicher, D., MNRAS, 443, 2410-2425
- Fontes, C. J., Fryer, C. L., Hungerford, A. L., et al., ArXiv e-prints, arXiv:1702.02990
- Furlanetto, S. R., Oh, S. P., & Briggs, F. H., Phys. Rep., 433, 181-301
- Habouzit, M., Volonteri, M., Latif, M., Dubois, Y., & Peirani, S., MNRAS, 463, 529-540
- Harker, G., Cole, S., Helly, J., Frenk, C., & Jenkins, A., MNRAS, 367, 1039-1049
- Heger, A., Fryer, C. L., Woosley, S. E., Langer, N., & Hartmann, D. H., ApJ, 591, 288-300
- Heger, A., & Woosley, S. E., ApJ, 567, 532-543
- , ApJ, 567, 532-543
- Hirano, S., Hosokawa, T., Yoshida, N., Omukai, K., & Yorke, H. W., MNRAS, 448, 568-587
- Hirano, S., Hosokawa, T., Yoshida, N., et al., ApJ, 781, 60
- Hopkins, A. M., & Beacom, J. F., ApJ, 651, 142-154
- Hosokawa, T., Hirano, S., Kuiper, R., et al., ApJ, 824, 119
- Hosokawa, T., Omukai, K., Yoshida, N., & Yorke, H. W., Science, 334, 1250
- Hsiao, E. Y., Conley, A., Howell, D. A., et al., ApJ, 663, 1187-1200
- Hummel, J. A., Pawlik, A. H., Milosavljević, M., & Bromm, V., ApJ, 755, 72
- Iben, Jr., I., & Tutukov, A. V., ApJ, 284, 719-744

- Illingworth, G., Magee, D., Bouwens, R., et al., ArXiv e-prints, arXiv:1606.00841
- Jansen, R. A., Webb Medium Deep Fields IDS GTO Team, & the NEPTDS-Chandra Team, t. N.-V. T. American Astronomical Society Meeting Abstracts, Vol. 230, American Astronomical Society Meeting Abstracts, 216.02
- Joggerst, C. C., Almgren, A., Bell, J., et al., ApJ, 709, 11-26
- Joggerst, C. C., & Whalen, D. J., ApJ, 728, 129
- Johnson, J. L., Greif, T. H., Bromm, V., Klessen, R. S., & Ippolito, J., MNRAS, 399, 37-47
- Johnson, J. L., Whalen, D. J., Even, W., et al., ApJ, 775, 107
- Johnson, J. L., Whalen, D. J., Fryer, C. L., & Li, H., ApJ, 750, 66
- Johnson, J. L., Whalen, D. J., Li, H., & Holz, D. E., ApJ, 771, 116
- Kalogera, V., Kim, C., Lorimer, D. R., et al., ApJ, 601, L179-L182
- , ApJ, 614, L137-L138
- Karlsson, T., Bromm, V., & Bland-Hawthorn, J., Reviews of Modern Physics, 85, 809-848
- Kasen, D., Fernández, R., & Metzger, B. D., MNRAS, 450, 1777-1786
- Kasen, D., Woosley, S. E., & Heger, A., ApJ, 734, 102
- Kashiyama, K., & Inayoshi, K., ApJ, 826, 80
- Khandrika, H., Burgasser, A. J., Melis, C., et al., AJ, 145, 71
- Kim, C., Perera, B. B. P., & McLaughlin, M. A., MNRAS, 448, 928-938
- Kulkarni, S. R., ArXiv Astrophysics e-prints, astro-ph/0510256

- Kumar, P., & Zhang, B., *Phys. Rep.*, 561, 1-109
- Lattimer, J. M., Mackie, F., Ravenhall, D. G., & Schramm, D. N., *ApJ*, 213, 225-233
- Lattimer, J. M., & Schramm, D. N., *ApJ*, 192, L145-L147
- Leloudas, G., Schulze, S., Krühler, T., et al., *MNRAS*, 449, 917-932
- Li, L.-X., & Paczyński, B., *ApJ*, 507, L59-L62
- Lodato, G., & Natarajan, P., *MNRAS*, 371, 1813-1823
- Loeb, A., & Furlanetto, S. R., *The First Galaxies in the Universe*
- Loeb, A., & Rasio, F. A., *ApJ*, 432, 52-61
- Lunnan, R., Chornock, R., Berger, E., et al., *ApJ*, 787, 138
- , *ArXiv e-prints*, arXiv:1708.01619
- Mackey, J., Bromm, V., & Hernquist, L., *ApJ*, 586, 1-11
- Maeder, A., & Meynet, G., *Reviews of Modern Physics*, 84, 25-63
- Magg, M., Hartwig, T., Glover, S. C. O., Klessen, R. S., & Whalen, D. J., *MNRAS*, 462, 3591-3601
- Matthee, J., Sobral, D., Santos, S., et al., *MNRAS*, 451, 400-417
- McKee, C. F., & Tan, J. C., *ApJ*, 681, 771-797
- Mesler, R. A., Whalen, D. J., Smidt, J., et al., *ApJ*, 787, 91
- Metzger, B. D., *Living Reviews in Relativity*, 20, 3
- Metzger, B. D., & Berger, E., *ApJ*, 746, 48

- Metzger, B. D., Martínez-Pinedo, G., Darbha, S., et al., MNRAS, 406, 2650-2662
- Montero, P. J., Janka, H.-T., & Müller, E., ApJ, 749, 37
- Moster, B. P., Naab, T., & White, S. D. M., ArXiv e-prints, arXiv:1705.05373
- Mould, J., Abbott, T., Cooke, J., et al., Science Bulletin, Volume 62, Issue 10, pp. 675-678,
62, 675-678
- Mutch, S. J., Geil, P. M., Poole, G. B., et al., MNRAS, 462, 250-276
- Natarajan, P., Pacucci, F., Ferrara, A., et al., ApJ, 838, 117
- Nicholl, M., Williams, P. K. G., Berger, E., et al., ApJ, 843, 84
- Nomoto, K., Tanaka, M., Tominaga, N., & Maeda, K., New Astronomy Reviews, 54,
191-200
- Nugent, P., Baron, E., Branch, D., Fisher, A., & Hauschildt, P. H., ApJ, 485, 812-819
- Oesch, P. A., Bouwens, R. J., Illingworth, G. D., et al., ApJ, 808, 104
- O’Shea, B. W., Wise, J. H., Xu, H., & Norman, M. L., ApJ, 807, L12
- Ouchi, M., Shimasaku, K., Furusawa, H., et al., ApJ, 723, 869-894
- Pacucci, F., Ferrara, A., Grazian, A., et al., MNRAS, 459, 1432-1439
- Pacucci, F., Ferrara, A., Volonteri, M., & Dubus, G., MNRAS, 454, 3771-3777
- Pacucci, F., Pallottini, A., Ferrara, A., & Gallerani, S., MNRAS, 468, L77-L81
- Pallottini, A., Ferrara, A., Pacucci, F., et al., MNRAS, 453, 2465-2470
- Pan, T., Kasen, D., & Loeb, A., MNRAS, 422, 2701-2711

- Pawlik, A. H., Milosavljević, M., & Bromm, V., *ApJ*, 731, 54
- Planck Collaboration, Ade, P. A. R., Aghanim, N., et al., *A&A*, 594, A17
- Postman, M., Coe, D., Benítez, N., et al., *ApJS*, 199, 25
- Prajs, S., Sullivan, M., Smith, M., et al., *MNRAS*, 464, 3568-3579
- Quimby, R. M., Yuan, F., Akerlof, C., & Wheeler, J. C., *MNRAS*, 431, 912-922
- Rakavy, G., & Shaviv, G., *ApJ*, 148, 803-+
- Recchi, S., Wünsch, R., Palouš, J., & Dinnbier, F., *Ap&SS*, 362, 183
- Renzini, A., *MNRAS*, 469, L63-L67
- Robertson, B. E., & Ellis, R. S., *ApJ*, 744, 95
- Robertson, B. E., Ellis, R. S., Dunlop, J. S., McLure, R. J., & Stark, D. P., *Nature*, 468, 49-55
- Rydberg, C. E., Zackrisson, E., & Scott, P. Cosmic Radiation Fields: Sources in the early Universe (CRF 2010), ed. M. Raue, T. Kneiske, D. Horns, D. Elsaesser, & P. Hauschildt , 26
- Safronek-Shrader, C., Milosavljević, M., & Bromm, V., *MNRAS*, 438, 1669-1685
- Shang, C., Bryan, G. L., & Haiman, Z., *MNRAS*, 402, 1249-1262
- Shivvers, I., Zheng, W., Van Dyk, S. D., et al., *MNRAS*, 471, 4381-4397
- Smidt, J., Whalen, D. J., Chatzopoulos, E., et al., *ApJ*, 805, 44
- Smidt, J., Whalen, D. J., Johnson, J. L., & Li, H., [arXiv:1703.00449](https://arxiv.org/abs/1703.00449), [arXiv:1703.00449](https://arxiv.org/abs/1703.00449)
- Smidt, J., Whalen, D. J., Wiggins, B. K., et al., *ApJ*, 797, 97

- Smidt, J., Wiggins, B. K., & Johnson, J. L., *ApJ*, 829, L6
- Smit, R., Bouwens, R. J., Labbé, I., et al., *ApJ*, 784, 58
- Smith, B. D., & Sigurdsson, S., *ApJ*, 661, L5-L8
- Sobral, D., Matthee, J., Darvish, B., et al., *ApJ*, 808, 139
- Stacy, A., Greif, T. H., & Bromm, V., *MNRAS*, 422, 290-309
- Stark, D. P., Richard, J., Charlot, S., et al., *MNRAS*, 450, 1846-1855
- Stark, D. P., Walth, G., Charlot, S., et al., *MNRAS*, 454, 1393-1403
- Sugimura, K., Omukai, K., & Inoue, A. K., *ArXiv e-prints*, arXiv:1407.4039
- Sullivan, M., Treyer, M. A., Ellis, R. S., et al., *MNRAS*, 312, 442-464
- Symbalisty, E., & Schramm, D. N., *Astrophys. Lett.*, 22, 143-145
- Tanaka, M., *Advances in Astronomy*, 2016, 634197
- Tanaka, M., Moriya, T. J., & Yoshida, N., *MNRAS*, 435, 2483-2493
- Trenti, M., Perna, R., & Tacchella, S., *ApJ*, 773, L22
- Umeda, H., Hosokawa, T., Omukai, K., & Yoshida, N., *ApJ*, 830, L34
- Volonteri, M., Lodato, G., & Natarajan, P., *MNRAS*, 383, 1079-1088
- Volonteri, M., & Rees, M. J., *ApJ*, 633, 624-629
- Whalen, D., Abel, T., & Norman, M. L., *ApJ*, 610, 14-22
- Whalen, D., van Veelen, B., O’Shea, B. W., & Norman, M. L., *ApJ*, 682, 49-67
- Whalen, D. J., *Acta Polytechnica*, 53, 573

- Whalen, D. J., & Fryer, C. L., *ApJ*, 756, L19
- Whalen, D. J., Fryer, C. L., Holz, D. E., et al., *ApJ*, 762, L6
- Whalen, D. J., Joggerst, C. C., Fryer, C. L., et al., *ApJ*, 768, 95
- Whalen, D. J., Johnson, J. L., Smidt, J., et al., *ApJ*, 777, 99
- , *ApJ*, 774, 64
- Whalen, D. J., Smidt, J., Even, W., et al., *ApJ*, 781, 106
- Whalen, D. J., Smidt, J., Johnson, J. L., et al., *arXiv:1312.6330*, *arXiv:1312.6330*
- Whalen, D. J., Even, W., Frey, L. H., et al., *ApJ*, 777, 110
- Whalen, D. J., Even, W., Smidt, J., et al., *ApJ*, 778, 17
- Whalen, D. J., Even, W., Lovekin, C. C., et al., *ApJ*, 768, 195
- Wise, J. H., Turk, M. J., Norman, M. L., & Abel, T., *ApJ*, 745, 50
- Woods, T. E., Heger, A., Whalen, D. J., Haemmerlé, L., & Klessen, R. S., *ApJ*, 842, L6
- Woosley, S. E., *ApJ*, 836, 244
- Woosley, S. E., Blinnikov, S., & Heger, A., *Nature*, 450, 390-392
- , *Nature*, 450, 390-392
- Woosley, S. E., Heger, A., & Weaver, T. A., *Reviews of Modern Physics*, 74, 1015-1071
- Xu, H., Norman, M. L., O’Shea, B. W., & Wise, J. H., *ApJ*, 823, 140
- Yajima, H., & Khochfar, S., *MNRAS*, 467, L51-L55
- Yoon, S.-C., Dierks, A., & Langer, N., *A&A*, 542, A113

Yoon, S.-C., Langer, N., & Norman, C., *A&A*, 460, 199-208

Yue, B., Ferrara, A., Salvaterra, R., Xu, Y., & Chen, X., *MNRAS*, 433, 1556-1566

Appendix: Pop III SNe

An extensive campaign of radiation hydrodynamical simulations has shown that PI SNe, PPI SNe and Type IIn SNe will be visible to *JWST* and the extremely large telescopes (ELTs) at $z \gtrsim 20$ (Whalen et al. 2013a,f,h, 2014). CC SNe will be visible to these telescopes at $z = 10$ – 20 (Whalen et al. 2013b) and rotating PI SNe and hypernovae will be visible out to $z \sim 10$ (Smidt et al. 2014, 2015). NIR light curves for 150 – $250 M_{\odot}$ PI SNe and 15 – $40 M_{\odot}$ CC SNe are shown in Figure 20. These studies demonstrate that the optimum wavelengths for observing SNe at $z = 10$ – 20 are 2 – $5 \mu\text{m}$. *JWST* is uniquely qualified to detect these events because its 40 K temperatures and low thermal noise vastly simplify its systematics in comparison to ground-based ELTs, which must contend with much greater instrument noise and atmospheric transmission in the NIR.

This manuscript was prepared with the AAS L^AT_EX macros v5.2.

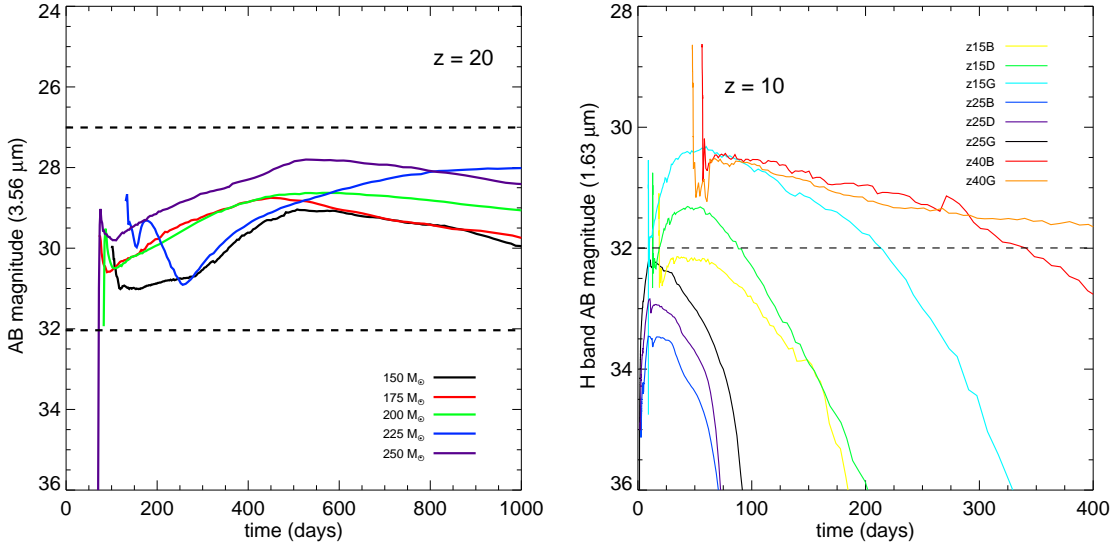


Fig. 20.— Left panel: light curves for 150, 175, 200, 225 and 250 M_{\odot} Pop III PI SNe at $z = 20$ at 3.56 μm . Right panel: light curves for 15, 25, and 40 M_{\odot} CC SNe at $z = 10$ at 1.63 μm . Here, the explosion energies are 0.6 foe (B series), 1.2 foe (D series), and 2.4 foe (G series), where 1 foe = 10^{51} erg.

Detections of both PI and CC SN, whose light curves are easily distinguishable, would enable a rough IMF to be built up over time as more events are found and binned by progenitor mass. Since both types of explosion are needed to do this, *JWST* will only be able to probe the IMF of early stars up to $z \sim 15$ unless gravitational lensing reveals CC SNe at higher redshifts (Pan et al. 2012; Whalen et al. 2013e). The possibility that lensed CC SNe could extend constraints on the Pop III IMF up to $z \sim 20$, the era of first light, may warrant the inclusion of a number of galaxy cluster lenses with large Einstein radii in the proposed field. Twenty five such clusters have now been studied in the CLASH and Frontier Fields programs by *HST* (Postman et al. 2012). Absent such detections, the discovery of PI SNe alone by *JWST* above $z \sim 15$ would still determine if primordial star formation led to stellar masses in excess of $\sim 100 M_{\odot}$ and place upper limits on global

SFRs at this epoch.

The main challenge to finding high-redshift transients is their low surface densities, which require large fields. Since cosmic SFRs inferred from observations of GRBs and low-luminosity, high-redshift galaxies have only been extrapolated up to $z = 15$ (Robertson & Ellis 2012), one must resort to numerical simulations for estimates of SFRs at earlier times. As shown in the left panel of Figure 21, these rates vary by a factor of 300 at the highest redshifts, highlighting the present uncertainties in them. However, even at $z \sim 20\text{--}25$, *JWST* is predicted to find a number of PI SNe (right panel of Figure 21; Hummel et al. 2012). The optimal search strategy is a mosaic approach with only modestly deep individual exposures. Our proposed field is well suited to push into this wide-field regime to place constraints on the SFR density of massive Pop III stars.

However, even the unlikely failure of *JWST* to harvest any transients in our FLARE field at $z \gtrsim 15$ would place useful, strong upper limits on global SFRs in the primordial Universe and could even shed light on the properties of dark matter. Models of early structure formation with warm dark matter predict a suppression of power on small scales that delays Pop III star formation to $z \sim 15$, so the failure to detect SNe at earlier times might be a signature of such suppression (Magg et al. 2016). Furthermore, any detections of SNe at $z \sim 10\text{--}20$ would still trace the rise of stellar populations in the first galaxies and put global SFRs on much firmer footing, even though they might not all be Pop III events due to chemical enrichment by the first SNe.

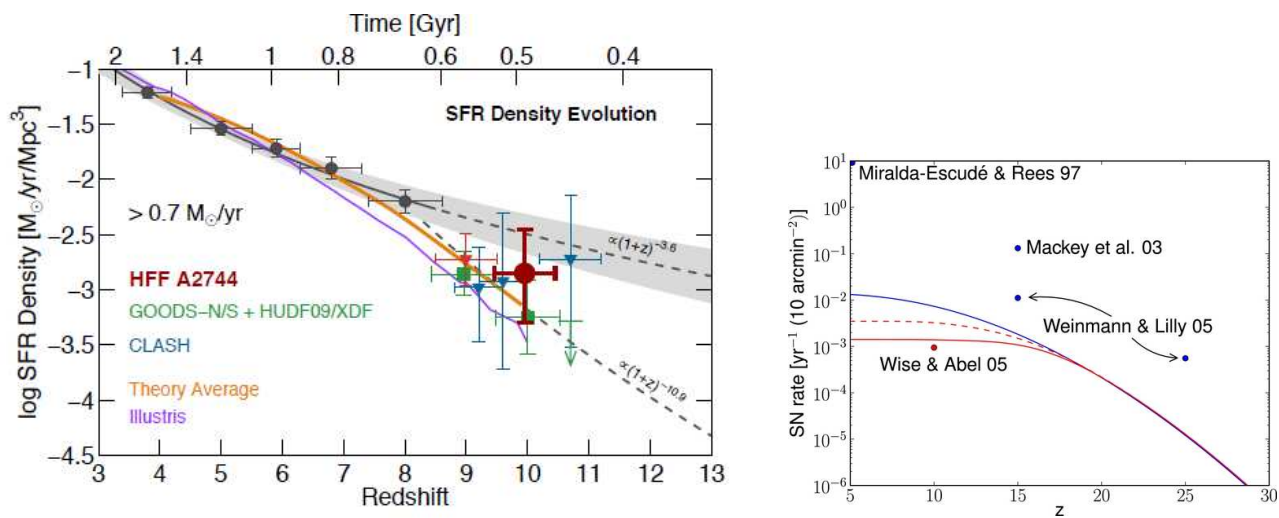


Fig. 21.— Global SFRs as a function of redshift (from Oesch et al. 2015). Two possible decline rates are shown. Right panel: PI SN rates in number per year per *JWST* field of view above a given redshift (Hummel et al. 2012). There are baryonic feedback mechanisms within the galactic halos where these massive stars form. We show the upper limit for weak feedback (blue line), strong feedback (red line), and an intermediate case (dashed red line). The symbols denote additional estimates from the literature.